

## THIRD-EPOCH MAGELLANIC CLOUD PROPER MOTIONS I: HST/WFC3 DATA AND ORBIT IMPLICATIONS

NITYA KALLIVAYALIL<sup>1,2</sup>, ROELAND P. VAN DER MAREL<sup>3</sup>, GURTINA BESLA<sup>4</sup>, JAY ANDERSON<sup>3</sup>, CHARLES ALCOCK<sup>5</sup>

ACCEPTED TO APJ: Jan 2, 2013

### ABSTRACT

We present proper motions for the Large & Small Magellanic Clouds (LMC & SMC) based on three epochs of *Hubble Space Telescope* data, spanning a  $\sim 7$  yr baseline, and centered on fields with background QSOs. The first two epochs, the subject of past analyses, were obtained with ACS/HRC, and have been reanalyzed here. The new third epoch with WFC3/UVIS increases the time baseline and provides better control of systematics. The three-epoch data yield proper motion random errors of only 1–2% per field. For the LMC this is sufficient to constrain the internal proper motion dynamics, as will be discussed in a separate paper. Here we focus on the implied center-of-mass proper motions:  $\mu_{W,LMC} = -1.910 \pm 0.020$  mas yr<sup>-1</sup>,  $\mu_{N,LMC} = 0.229 \pm 0.047$  mas yr<sup>-1</sup>, and  $\mu_{W,SMC} = -0.772 \pm 0.063$  mas yr<sup>-1</sup>,  $\mu_{N,SMC} = -1.117 \pm 0.061$  mas yr<sup>-1</sup>. We combine the results with a revised understanding of the solar motion in the Milky Way to derive Galactocentric velocities:  $v_{tot,LMC} = 321 \pm 24$  km s<sup>-1</sup> and  $v_{tot,SMC} = 217 \pm 26$  km s<sup>-1</sup>. Our proper motion uncertainties are now dominated by limitations in our understanding of the internal kinematics and geometry of the Clouds, and our velocity uncertainties are dominated by distance errors. Orbit calculations for the Clouds around the Milky Way allow a range of orbital periods, depending on the uncertain masses of the Milky Way and LMC. Periods  $\lesssim 4$  Gyr are ruled out, which poses a challenge for traditional Magellanic Stream models. First-infall orbits are preferred (as supported by other arguments as well) if one imposes the requirement that the LMC and SMC must have been a bound pair for at least several Gyr.

*Subject headings:* galaxies: interactions — galaxies: kinematics and dynamics — galaxies: evolution  
— Galaxy: structure — Magellanic Clouds

### 1. INTRODUCTION

High-precision proper motion (PM) measurements of the Large and Small Magellanic Clouds made by our group with two epochs of Hubble Space Telescope’s (*HST*) ACS High Resolution Camera (HRC) data (Kallivayalil et al. 2006a,b, hereafter **K2** & **K1**), and confirmed by Piatek et al. (2008, hereafter **P08**), have revolutionized the field of Magellanic Clouds research. The implied tangential velocities were high enough, approximately 100 km s<sup>-1</sup> higher than in previous theoretical models, and the observational errors were small enough ( $\sim 0.07$  mas yr<sup>-1</sup> for LMC), that an orbital solution in which the Clouds are either only now on their first infall about the Milky Way (MW) (Besla et al. 2007, hereafter **B07**), or are on an eccentric, long period ( $> 6$  Gyr) orbit (Shattow & Loeb 2009, **B07**) are the favored solutions. In addition, the observed relative velocity between the Clouds was of order the escape speed of the SMC from the LMC ( $105 \pm 42$  km s<sup>-1</sup>; see **K2**) leaving open the possibility that the Clouds may not be bound to each other, although bound orbits were still allowed

within the relatively large error bars which came from the less-precise SMC PM determination ( $\sim 0.18$  mas yr<sup>-1</sup>). These results received much attention from the community in part because they require a new formation mechanism for the Magellanic Stream, a young coherent stream of H I gas that trails the Clouds  $\sim 150^\circ$  across the sky (Wannier & Wrixon 1972; Mathewson et al. 1974; Putman et al. 2003; Brüns et al. 2005; Nidever et al. 2010). Most models, be they tidal or ram-pressure in nature, require multiple pericentric passages in order to be viable stripping mechanisms (Růžička et al. 2009; Bekki 2008; Connors et al. 2006; Mastrogiuseppe et al. 2005; Gardiner & Noguchi 1996; Moore & Davis 1994; Murai & Fujimoto 1980).

We have recently put forth an alternative formation mechanism for the Stream in which the material is removed by LMC tides acting on the SMC before the system falls into the MW for the first time (Besla et al. 2010). A firm prediction of this model is that the Clouds have been bound to each other and further that the SMC is on a highly eccentric, prograde orbit about the LMC ( $e = 0.7$ ; apocenter  $\sim 100$  kpc). This orbital configuration prevents the Clouds from merging and also leaves the dispersion-supported material within the SMC’s disk radius relatively unaffected, while resonances aid in removing rotationally supported material from the outskirts of the SMC’s disk. Thus, despite the large parameter space involved in modeling a feature such as the Stream, there are two pieces of information that can dramatically reduce the uncertainty in the models: 1) knowing whether the Clouds are on a short or long period orbit about

nitya.kallivayalil@yale.edu

<sup>1</sup> YCAA Prize Fellow, Yale Center for Astronomy & Astrophysics, 260 Whitney Ave, New Haven, CT 06511

<sup>2</sup> Dept. of Astronomy, University of Virginia, 530 McCormick Road, Charlottesville, VA 22904

<sup>3</sup> Space Telescope Science Institute, 3700 San Martin Drive, Baltimore, MD 21218

<sup>4</sup> Hubble Fellow, Columbia Astrophysics Laboratory, 1027 Pupin Hall, MC 5247, New York, NY 10027

<sup>5</sup> Harvard-Smithsonian Center for Astrophysics, 60 Garden Street, Cambridge, MA 02138

the MW, and 2) the orbital eccentricity of the SMC’s orbit about the LMC. We recently expanded on this work, building on earlier ideas of Yoshizawa & Noguchi (2003) and Bekki & Chiba (2005), arguing that the internal kinematics and structure of the LMC strongly favor a scenario in which the MCs have recently experienced a direct collision (Besla et al. 2012). We also looked more generally at the implications of such dwarf-dwarf interactions for Magellanic Irregulars, a class of dwarf galaxies for which the LMC is a prototype. We found that prograde dwarf-dwarf tidal interactions can efficiently remove baryons from the lower mass companion and that structures such as off-centered bars and one-armed spirals may be hallmarks of ongoing or recent interactions with a low mass companion (mass ratio 1:10).

Apart from our own work on the formation of the Stream, these PM measurements have spurred many other new theoretical investigations into the Clouds’ origin, whether from M31 or the far reaches of the Local Group (Shattow & Loeb 2009; Kallivayalil et al. 2009a; Yang & Hammer 2010). Attempts have been made to measure the Milky Way mass from the kinematic properties of the LMC (Kallivayalil et al. 2009a; Busha et al. 2011a; Boylan-Kolchin et al. 2011). Recent studies have attempted to place the orbits of the Magellanic Clouds in a cosmological context, looking at the expected infall times in a statistical sense, and favoring a scenario in which the Clouds are likely on their first infall into the MW (Boylan-Kolchin et al. 2011; Busha et al. 2011b, see also Bekki (2011)). Rocha et al. (2011) analyzed subhalos in the Via Lactea II cosmological simulation and find that present day orbital energies are tightly correlated with the time at which subhalos crossed into the host’s virial radius. Their analysis indicates that the LMC entered the MW virial radius  $\sim 4$  Gyr ago, in agreement with the Busha et al. (2011a) and Boylan-Kolchin et al. (2011) results.

Overall, the Busha et al. (2011a) and Boylan-Kolchin et al. (2011) works find different conclusions for the mass of the MW. This is because Busha et al. also folded in constraints on the separation between the Clouds and the MW host which yields posterior distributions that favor lower mass MW halos. The Boylan-Kochin et al. study favors MW models with a high mass because the K1 velocities imply the LMC is moving close to the escape speed of a  $10^{12}M_{\odot}$  halo. Since subhalos are rarely ever accreted on unbound orbits, this means that the Bayesian analysis will be weighted towards a higher mass. Consequently, they favor a MW mass in excess of  $2 \times 10^{12}M_{\odot}$ . Both studies represent a novel approach and new avenue for near-field cosmology, i.e., using accurate orbital kinematics/histories of MW satellites to constrain the properties of the MW. Because the speed is so close to the escape speed it is crucial that the velocity measurement be accurate for the LMC. A lower speed for the LMC would favor MW mass estimates between  $1-2 \times 10^{12}M_{\odot}$ .

In order to better address these questions about the Clouds’ velocities and likely orbits, we obtained an additional epoch of *HST* data with the Wide Field Camera 3 (WFC3). With measurement errors similar to those in epochs 1 & 2, and an increased time baseline from 2 to 7 yrs, this allows for decreased PM errors by a factor

of a few. In turn, this yields improved knowledge of the past orbit. Moreover, a third epoch provides a valuable check on systematic errors: there is always a straight line between two points, but if a third point, particularly obtained with a completely different detector, fails to line up then that is a clear sign of errors in the analysis.

In this paper we present the results from the analysis of the third epoch of *HST* data of the Magellanic Clouds, and the implications for their space motion and past orbit. In §2 we discuss the details of the observations, the analysis of the WFC3 data, an improved reanalysis of the ACS data, and the resulting two-epoch and three-epoch PMs. In §3 we derive the PMs of the LMC and SMC Center of Mass (COM) from the measurements of the individual fields. In §4 we compare the new results to previously reported measurements and estimates. In §5 we discuss the corresponding space motions of the Clouds. In §6 we discuss the implications for the orbits of the Clouds, and the new insights and improvements thus obtained. The main conclusions are summarized and discussed in §7. Appendices discuss some additional *HST* data that we obtained, but which are not included in the present study.

In a companion Paper II we use the new LMC data to study its PM rotation field. This provides new insights into the distance, center, orientation, and rotation of the LMC disk. The COM motions derived in the present paper use the field dependent corrections derived in Paper II.

## 2. DATA & ANALYSIS

### 2.1. Description of Observations

Geha et al. (2003) identified a total of 54 QSOs behind the Clouds from their optical variability in the MACHO database. These QSOs provided the inertial reference frame against which the PM measurements were made over a 2 yr baseline in K1 & K2, based on observations obtained between August 2002 and June 2005. For most efficient use of *HST* resources we decided to observe in SNAPSHOT mode for both epochs. Our two SNAP programs of imaging with the HRC achieved an overall completion rate of 48% yielding a final sample of 21 QSOs behind the LMC and 5 behind the SMC.

We obtained an additional epoch of data during the period July 2007 to November 2008. These observations executed with the HST WFPC2 camera, due to the failure of ACS at that time. We briefly describe these data in Appendix A, but due to their limited quality, we don’t use them in the analysis presented here.

We obtained another epoch of data with the HST WFC3 camera during the period October 2009 to July 2010. These observations also executed in SNAPSHOT mode, and we refer to them as the “third epoch”. The final yield from this program was 11 observed QSO fields for the LMC and 4 observed QSO fields for the SMC. However, two QSO fields, one in each galaxy, proved unsuitable for PM determinations. As discussed in Appendix B, in one field the QSO showed a bright extended host galaxy, which complicates astrometry, and in the other field the nature of the QSO was not confirmed. These two fields are omitted from the subsequent discussion and analysis. Therefore, the final number of QSOs used for the three-epoch analysis is 10 for the LMC and

3 for the SMC.

The HRC data, which makes up the first two epochs of this study, is discussed in detail in K1. Briefly, for our main astrometry goals we chose the F606W filter which is a broad  $V$  filter with high throughput. Eight dithered exposures were taken in each epoch to minimize pixelization-related systematic errors, and the dither pattern was kept the same over the two epochs. Exposure times were chosen so as to achieve a  $S/N$  of at least 100 for the QSOs based on the known MACHO magnitudes at the time.

For the third epoch with WFC3/UVIS (PID 11730), we again used the F606W filter and used the 4-point DITHER-BOX pattern which is made for optimal sampling of the PSF. We aimed at  $S/N \sim 200$  for the QSOs in order to match the astrometric quality of the ACS data. Even though the WFC3/UVIS pixels are bigger than ACS/HRC pixels, with adequate dithering this should not degrade the astrometry because the astrometric error is proportional to the  $(FWHM/SNR)$  of the target. With QSO brightnesses in the epoch 1 sample ranging from  $16.5 \leq V \leq 22.0$ , and an average brightness of  $V = 19.5$ , this yielded total science exposure times for epoch 3 ranging from 2.6 to 17.7 minutes, with an average of 12 minutes. Tables 1 & 2 describe the combined three-epoch dataset, including RA/DECs for the QSOs, whether they were observed with WFC3 or not, the total WFC3 exposure times, and the corresponding time baseline for the PM measurement.

Figure 1 shows the locations of the QSOs behind the LMC and SMC. QSOs for which we obtained two epochs of data are marked with yellow diamonds. Their distribution behind the LMC is sparse but reasonably uniform. QSOs observed with the WFC3 are marked with red squares. Note that there is 1 “new” LMC field for which there is only first epoch ACS and third epoch WFC3 data.

### 2.2. Analysis of WFC3/UVIS Data

As in K1 & K2, we used the bias-subtracted, dark-subtracted, flat-fielded images (`.flt.fits`) provided by the STScI data reduction pipeline for our basic reduction purposes. Anderson & King (2004) found that these images are well-behaved astrometrically. They are not, however, corrected for geometric distortion. We did not use the geometrically corrected products created by the MultiDrizzle software (`_drz.fits`) since they involve a re-sampling that might degrade the astrometry. Instead of geometrically correcting the images, we geometrically corrected the positions that we measured on the images. The positions were measured by means of empirical PSFs constructed from other data sets (similar to the approach discussed by Anderson & King 2006 in ACS/ISR 06-01). The geometric corrections were performed according to Bellini et al. (2011). In their study, the geometric distortion is modeled with two components: a third-order polynomial and an empirically-derived look-up table for the residuals, one per chip and filter combination. The method is akin to that used in Anderson & King (2004) and is shown in Bellini et al. (2011) to be stable over time to better than 0.008 pixels (RMS) in each coordinate.

Since we are performing relative astrometry we have freedom in constructing the masterframe (per QSO field) into which all relevant star positions are to be trans-

formed. While PSF-fitting was performed on the `flt` images, we did use stars in the `drz` image as a starting point to defining our masterframe, because their WCS header information is the most accurate. Simple aperture photometry was performed on the `drz` image to obtain initial positions and magnitudes for real sources in the region of overlap of all 4 individual exposures with orientation North up and East to the left. We then did a simple transformation of these initial positions to an  $(x, y)$ -frame of identical orientation, but with a chosen center and 25 mas pixels (for simplicity). A six-parameter linear transformation for the 4 individual `flt` WFC3 exposures into this frame was then calculated. Based on previous experience, we only use stars brighter than an instrumental magnitude,  $M_{\text{INSTR}} = -8$  ( $S/N \sim 40$ ). The instrumental magnitude is defined as  $-2.5 \log(\text{counts})$  in the F606W `flt` image (without application of a zero-point). We then calculated a new masterframe position for each source by averaging the linearly transformed WFC3 positions. At this stage we iterated on the linear transformations, using only stars with measurement errors smaller than  $\sim 0.1$  pixels, that are common to all 4 WFC3 exposures. The positional errors are calculated as the RMS scatter between multiple measurements of the same source.

In general, we can routinely center WFC3 stars to 0.02 pixels. Because our exposures are deeper and the FOV is much larger than for ACS/HRC, we identify on average  $\sim 200 - 800$  sources in the WFC3 images, depending on the field. By contrast there are far fewer sources in the HRC fields.

### 2.3. Re-analysis of ACS/HRC Data

In our original K1 analysis we argued, based on detailed calculations and consistency checks, that the degrading charge transfer efficiency (CTE) of the HRC was not expected to systematically affect our analysis. The main reason was that the SNAP nature of the program yielded random roll angles of the telescope for each QSO field. Given that we had  $N = 21$  QSO fields with more or less random detector orientations on the sky, any CTE induced astrometric shift along columns would average down to zero  $\propto N^{-1/2}$ . There is no explicit model for the underlying HRC CCD detector physics and charge trap properties, as there now is for other cameras (Anderson & Bedin 2010). The residual CTE effects, given the random roll angles of our exposures, would be expected to puff up the final RMS of the measurements. We included this effect by using the RMS scatter between fields as our final error estimates, instead of simply propagating the per-field weighted errors (which would have suggested a factor of 2 higher accuracy).

In K1, our final PM value was based on 13 fields that we deemed as high quality for various reasons, and because of this reduced number of fields, and the small number of total SMC fields, CTE issues remained a legitimate concern. P08 subsequently performed an independent re-analysis of our HRC data and used a simple correction for CTE that was a function of  $Y$  coordinate of the object, the time since installation, and  $\propto S/N^{-0.42}$ . This latter exponent came from the ACS Handbook. They found, as expected, that correcting for CTE did not have a large systematic effect on the anal-

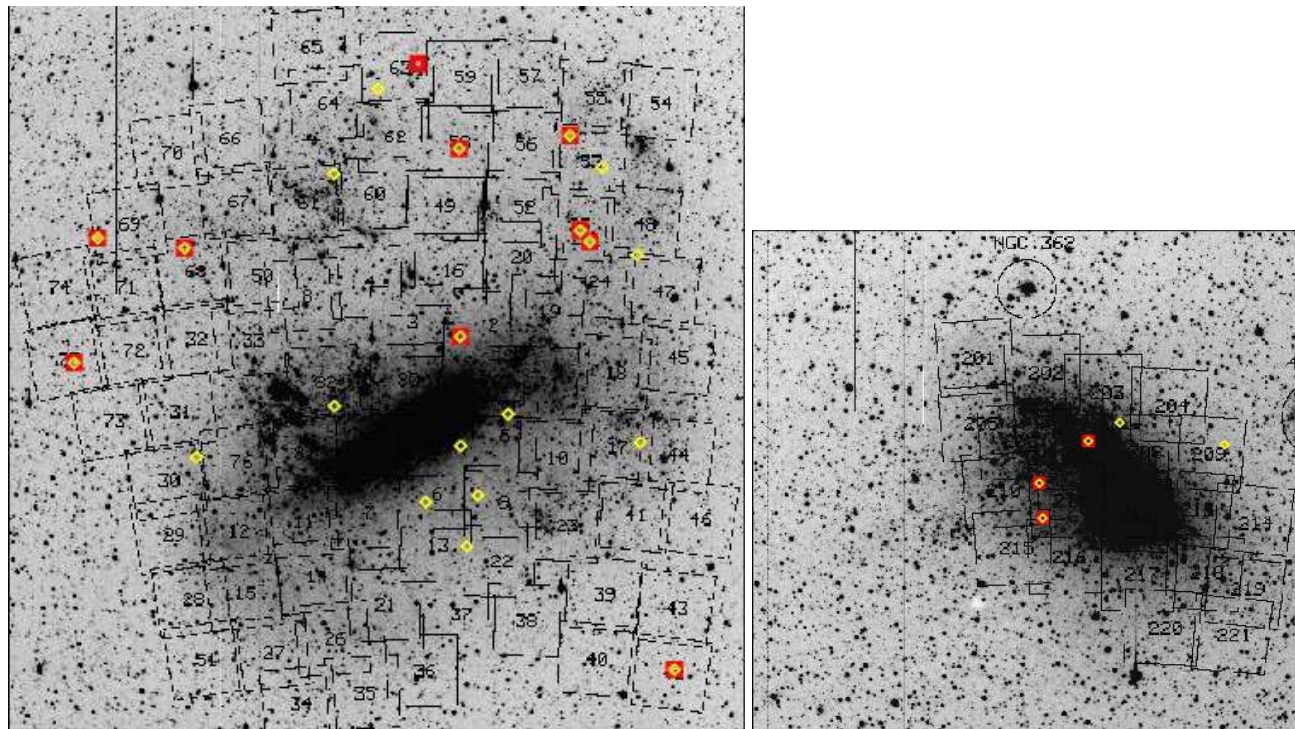


**Figure 1.** *R*-band image of the LMC ( $8^\circ \times 8^\circ$ ), and the SMC ( $3^\circ \times 5^\circ$ ). The MACHO photometric coverage is indicated. Red squares indicate reference QSOs with WFC3 data and yellow diamonds indicate those with two epochs of ACS data.

ysis (they obtained a COM PM for the LMC within  $1\sigma$  from that of K1). However, they did obtain better field-to-field agreement. This yielded smaller error bars on the COM motion, and the possibility to derive a rudimentary PM rotation curve.

For the present study we reanalyzed the HRC data using our own new prescription for CTE degradation as well as other improvements. The main differences in this reanalysis versus the analysis in K1 & K2 are: (1) we use new codes for the implementation of 6-parameter linear transformations between the two epochs that employ error-weighting for the stars. In the previous analysis we only used rejection. (2) We employ a prescription to correct for CTE, the form for which is as follows:

$$y_{\text{NEW}} = y_{\text{RAW}} - \left( \alpha \times \frac{y}{1024.0} \times \frac{t}{365.25} \times \frac{\text{MAX}[(M_{\text{INSTR}} - M_{\text{INSTR,lim}}), 0]}{\text{norm}} \right), \quad (1)$$

where  $y$  is the measured position of a star on the detector,  $M_{\text{INSTR}}$  is the instrumental magnitude, typically ranging from  $M_{\text{INSTR}} = -6$  (faintest) to  $-12$  (brightest) in our data, and  $t$  is the time since installation of ACS (Modified Julian Date = 52333). CTE affects faint stars more than bright stars, and stars brighter than  $M_{\text{INSTR,lim}}$  are assumed to be unaffected. Norm is simply a normalizing factor discussed below. The slope,  $\alpha$ , was fit in the following fashion: we sequentially corrected averaged detector  $y$  positions by a range of slopes. After application of the correction of a given slope, error-weighted transformations were calculated for stars from epoch 2 into the epoch 1 frame. The input error per epoch is the  $\text{RMS}/\sqrt{N}$  obtained from centering the star over  $N$  exposures in that epoch. We then calculated what

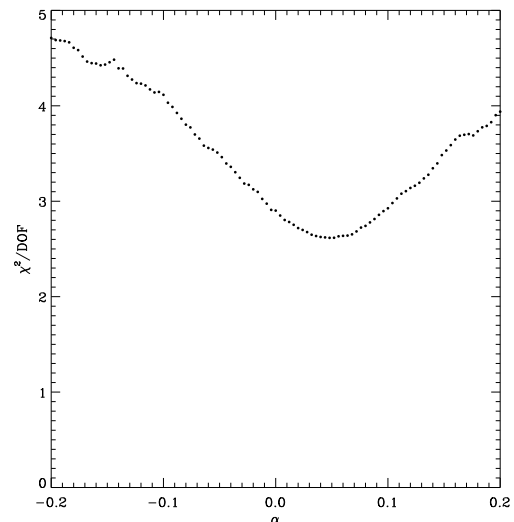


**Figure 2.** The total  $\chi^2/\text{DOF}$  for all the QSO fields as a function of CTE slope  $\alpha$  (see Equation 1), for  $M_{\text{INSTR,lim}} = -10$  and  $\text{norm} = 4$ . The minimum indicates the value of  $\alpha$  that provides the best correction.

slope gave the minimum total  $\chi^2/\text{DOF}$  for these transformations summed over all 21 QSO fields, where DOF stands for degrees of freedom, and is defined as follows:  $N_{\text{DOF}} = N_{\text{data}} - N_{\text{param}}$ , where  $N_{\text{data}}$  is twice the number of fields and  $N_{\text{param}}$  is the number of free parameters optimized in the fit. The QSO is not included in these transformations.

Figure 2 shows the total  $\chi^2/\text{DOF}$  for all the QSO fields as a function of  $\alpha$ . We tried several  $M_{\text{INSTR,lim}}$  limits,  $M_{\text{INSTR,lim}} = (-10, -11, -12)$ , where  $-12$  corresponds roughly to the brightest stars in the field. We

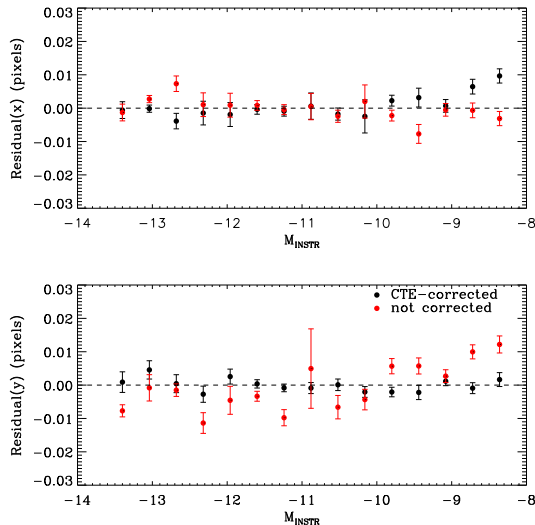


**Figure 3.** Residual star PMs (pix) after CTE correction via Equation (1) as a function of  $M_{\text{INSTR}}$  (black symbols) and plotted in the ACS e1 frame, i.e.  $x$  and  $y$  are in the native detector directions. The pixel scale is 28 mas/pix. Stars from all fields were binned together. The average PM should be zero by construction. Remaining trends are indicative of systematic errors. Points in red show the results without application of CTE corrections.

normalized the magnitude correction such that it is the greater of zero, when a star is brighter than or equal to  $-12$ , or a fractional correction up to a size of approximately 1, for  $M_{\text{INSTR}} = -6$  to  $-12$ . Therefore, for  $M_{\text{INSTR,lim}} = (-10, -11, -12)$ , the corresponding values for norm are (4, 5, 6). This range of  $M_{\text{INSTR,lim}}$  did not affect the final PM values by more than  $1\sigma$ . In addition to fitting for CTE-slope, we tried a number of different faint end magnitude cut-offs for the stars used in the transformations, settling on only using stars brighter than  $M_{\text{INSTR}} = -8$ . We also employed rejection in the form of ( $|\text{residual}/\text{error}| < 3$ ), i.e. a cut based on the size of the residual of the transformation of a star divided by its measurement error.

As a consistency check, we calculated the residual in pixels for each Magellanic Cloud star between epoch 2 and epoch 1. This PM should be zero on average, since differential streaming motions *within* each field are too small to be resolved by our measurements. We averaged the  $y$ -residuals over all stars in all QSO fields, and binned the results by  $M_{\text{INSTR}}$ . The QSO was again excluded. Figure 3 shows the results. Points in red correspond to  $\alpha = 0$  (i.e., no CTE-correction applied). A clear trend with magnitude in the  $y$ -residuals reveals CTE-induced astrometric shifts. By contrast the black points are for our best-fit CTE-correction parameters in eq. (1), which are  $\alpha = 0.048$  for  $M_{\text{INSTR,lim}} = -10$  and  $\text{norm} = 4$ . There is no evidence for any remaining  $y$ -CTE trend larger than 0.003 pixels (i.e., smaller than our random errors). There is no indication that serial-transfer CTE in the  $x$ -direction might have significantly affected the analysis, so we do not apply any corrections for it.

#### 2.4. Two-epoch Proper Motions

From hereon we define the proper motion in the west ( $\mu_W$ ) and north ( $\mu_N$ ) directions in terms of the change in right ascension ( $\alpha$ ) and declination ( $\delta$ ) on the sky:

$\mu_W \equiv -(d\alpha/dt) \cos(\delta)$ ,  $\mu_N \equiv d\delta/dt$ . With the final ACS to ACS transformation terms in hand, we determined the PM for each source, including the QSO. A linear function with time was fit to the available positions. The best-fit slope gives the PM. The average PM of the stars in each field is zero by construction. However, the QSO appears to move due to its reflex motion with respect to the LMC/SMC stars in the foreground. Hence, the average absolute PM of the stars in the field is simply minus the PM of the QSO. The final error in this PM has two components. One component is the error in the average PM of all the stars:  $\sigma_{(\text{PM})}$ <sup>6</sup>. This error quantifies how accurately we were able to align the star-fields between the epochs. This was added in quadrature to the formal error of the fit to the QSO's motion,  $\delta\text{PM}_{\text{QSO}}$ . So the error of a given field in either direction is  $\delta\mu_W$  or  $\delta\mu_N = \sqrt{\delta\text{PM}_{\text{QSO}}^2 + \sigma_{(\text{PM})}^2}$ .

Columns 7–10 of Tables 1 & 2 list the PMs thus inferred for all fields with two epochs of ACS data, and the associated errors, ( $\delta\mu_W, \delta\mu_N$ ). These results are very consistent with those of P08 even though we have used different methodologies for PSF-fitting, linear transformations and CTE-correction. The average residual between our reanalysis and that of P08 is 0.08 mas yr<sup>-1</sup> lower in the West direction and 0.06 mas yr<sup>-1</sup> lower in the North direction, while the  $\chi^2$  summed over all 21 fields is 12 in the West direction and 8 in the North direction. This is acceptable compared to  $N_{\text{DOF}}$ . The  $1\sigma$  difference between our final values and those of P08 arises from the inclusion of error-weighting in the transformations, and not the specifics of the CTE correction. If we exclude error-weighting, we recover values closer to P08. Since there are some sparse fields in which only a small number of stars are used in the transformations, it is especially important to include error-weighting in the analysis.

#### 2.5. Three-epoch Proper Motions

The inclusion of the WFC3 data gives us 20 images per QSO field for 15 fields: 8 ACS first epoch (e1), 8 ACS second epoch (e2), and 4 WFC3 third epoch (e3). One LMC field has only e1 and e3 data, and hence 12 images. To calculate PMs we first correct the ACS positions for CTE as in §2.3. We then perform preliminary transformations for stars (brighter than  $M_{\text{INSTR}} = -8$ ) in each of the 20 images into the masterframe defined in §2.2. All 20 resulting  $(x, y)$  centers of each star are averaged and the RMS is calculated to make up the final masterframe and error (the QSO positions are not averaged). We then treat this as the initial target frame for transformations. As the input frame, we use the individual positions of the stars in each of the 20 images, with input error the RMS per epoch. Again, as in §2.3, error-weighting, rejection, and iteration are used in the determination of the final transformation terms into the masterframe.

At this stage we lose the possible advantages of having such a large FOV and high number of sources in e3 because we are limited by the relatively sparse (and small) HRC fields. When we perform final transforma-

<sup>6</sup> Although the average is formally zero by construction, the precision of this zeropoint is limited by the measurement errors of the stars at the two epochs.

tions to put e1, e2 and e3 into the masterframe, we only use the sources that are common to the HRC. The number of sources used in the transformations, after all cuts, is listed in column 6 of Tables 1 & 2. The variation in this number reflects the real variation in stellar density at different locations in the Clouds and is not an artifact of the analysis.

Figure 4 shows the  $x$  vs.  $y$  (equivalent to  $W, N$ ) positions in pixels of the QSO, after transformation into the masterframe, for 4 randomly chosen QSO fields. The fields are labeled according to Tables 1 & 2. Linear motion is clearly visible, as is the consistency across the three epochs. Each triangle represents 1 of the 20 positions of the QSO relative to the starfield. The scatter reflects the real error in centering the QSO within a given epoch. In most cases the quality (RMS) of the WFC3 data is comparable to that of HRC as we expected based on the fact that we aimed for higher  $S/N$  in e3 to account for the larger pixels of the WFC3. This plot represents the reflex motion of the L/SMC. The actual PM and its random error were determined as described in §2.4 by fitting linear motion with time to all sources. The high quality of the results is visible by eye in Figure 4. For two of the LMC fields in Figure 4 we also show the  $x$  and  $y$  position in pixels of the QSO as a function of time in Figure 5. The corresponding linear fits are also shown.

Columns 11–14 of Tables 1 & 2 list the PMs thus inferred for all fields with both ACS and WFC3 data, and the associated errors,  $(\delta\mu_W, \delta\mu_N)$ .

### 3. PROPER MOTION RESULTS

#### 3.1. Comparison of Two-Epoch and Three-epoch PMs

In Figures 6 and 7(*top*) we show the measured QSO motions (colored symbols) in the  $(\mu_W, \mu_N)$ -plane compared to the star motions (open circles; centered around zero by construction) for the LMC & SMC respectively. The stellar motions clearly separate from the QSO motions. The green filled circles show the results from linear fits to all three epochs of data, and the pink squares show results from §2.3 for e1 and e2 only. The fact that the averages are consistent with each other is visible by eye. The addition of a third epoch with a different *HST* instrument not only improves the accuracy of the measured PMs, but also demonstrates that there were no fundamental systematic problems with the earlier two-epoch analysis of the observations in K1, K2, and P08.

#### 3.2. LMC COM Motion

As discussed in K1, given the large size the LMC subtends on the sky and the fact that we know it possesses internal rotation, the motion observed for an individual QSO field must be written as:  $\text{PM}(\text{field}) = \text{PM}(\text{COM}) + \text{PM}_{\text{res}}(\text{field})$ . Here  $\text{PM}(\text{COM})$  is the proper motion of the LMC COM and  $\text{PM}_{\text{res}}(\text{field})$  is a field-dependent residual. The latter contains contributions from different effects: (a) variations as a function of position in the components of the three-dimensional velocity vector of the COM that are seen in the plane of the sky (“viewing perspective”), and (b) the internal rotation of the LMC (see formulae in van der Marel et al. 2002, hereafter **vdM02**). Both corrections make a similar contribution to the observed PMs. Given the location of our fields, the viewing perspective contributes

$\lesssim 0.4 \text{ mas yr}^{-1}$  and the internal LMC rotation contributes  $\lesssim 0.3 \text{ mas yr}^{-1}$ . This is less than  $\sim 20\%$  of the overall PM, but that is significant given the accuracy that we are trying to achieve.

The field-dependent residuals depend on the COM PM and vice-versa and hence we used an iterative procedure to evaluate them in K1. For the internal rotation model of the LMC we used the model of vdM02, based on the line-of-sight (LOS) velocity data for 1041 carbon stars. This was because our PMs themselves were not accurate enough to significantly constrain the LMC rotation model. P08 took a similar approach by leaving the LMC center and disk plane orientation fixed at the values found by vdM02. However, they did vary and fit the amplitude of the rotation curve.

With the addition of the WFC3 epoch, the per-field, per coordinate PM errors are now typically  $0.03 \text{ mas yr}^{-1}$  (see Table 1, columns 13 & 14), which is only  $\sim 7 \text{ km s}^{-1}$ . We show in Paper II that this provides enough information to independently constrain all parameters of the PM rotation field, without reference to prior knowledge from LOS velocity studies. Table 3 lists the results, and compares them to the values from vdM02 which were used by K1 and P08. We also compare them to the values from a more recent study by Olsen et al. (2011), who analyzed the LOS velocities of  $\sim 6000$  massive red supergiants, oxygen-rich and carbon-rich AGB stars. A detailed discussion of the commonalities and differences between the results is presented in Paper II. We summarize here only the salient features relevant to the determination of the LMC COM motion.

The inferred orientation of the LMC disk, as measured by the inclination  $i$  and the position angle  $\theta$  of the line of nodes, is consistent with the range of values previously reported using other methods (see reviews of van der Marel (2006) and van der Marel et al. (2009)). The rotation curve amplitude inferred from the PM data falls between those determined from the LOS velocities of (old) carbon stars (vdM02; Olsen & Massey 2007) and (young) red supergiants (Olsen et al. 2011, see Table 3). This is as expected, since the (bright) stars in our HST fields contain a mix of older and younger stars (see the color-magnitude diagram in Figure 6 of K1). This confirms the accuracy of the new PM data, both in a random and a systematic sense. The rotation curve amplitude inferred from our PM data is not, however, consistent with the result of P08. They were able to infer a rotation curve from the two-epoch data, but their rotation velocity was surprisingly high:  $120 \pm 15 \text{ km s}^{-1}$ . This is approximately 30–40  $\text{km s}^{-1}$  higher than the value derived from the LOS velocities of H I and red supergiants (Kim et al. 1998; Olsen et al. 2011). It would be particularly hard to understand how the stars in the LMC could be rotating significantly faster than the H I gas.

The most important difference between our new results from Paper II and the LOS study of vdM02 (used by K1 and P08) is in the position of the LMC center. In Paper II we find strong evidence that the center of the stellar PM rotation field is consistent with the position of the H I dynamical center. This makes theoretical sense, since the stars and gas are orbiting in the same gravitational potential. However, this result differs by  $1.12^\circ$  from the position advocated by vdM02, which

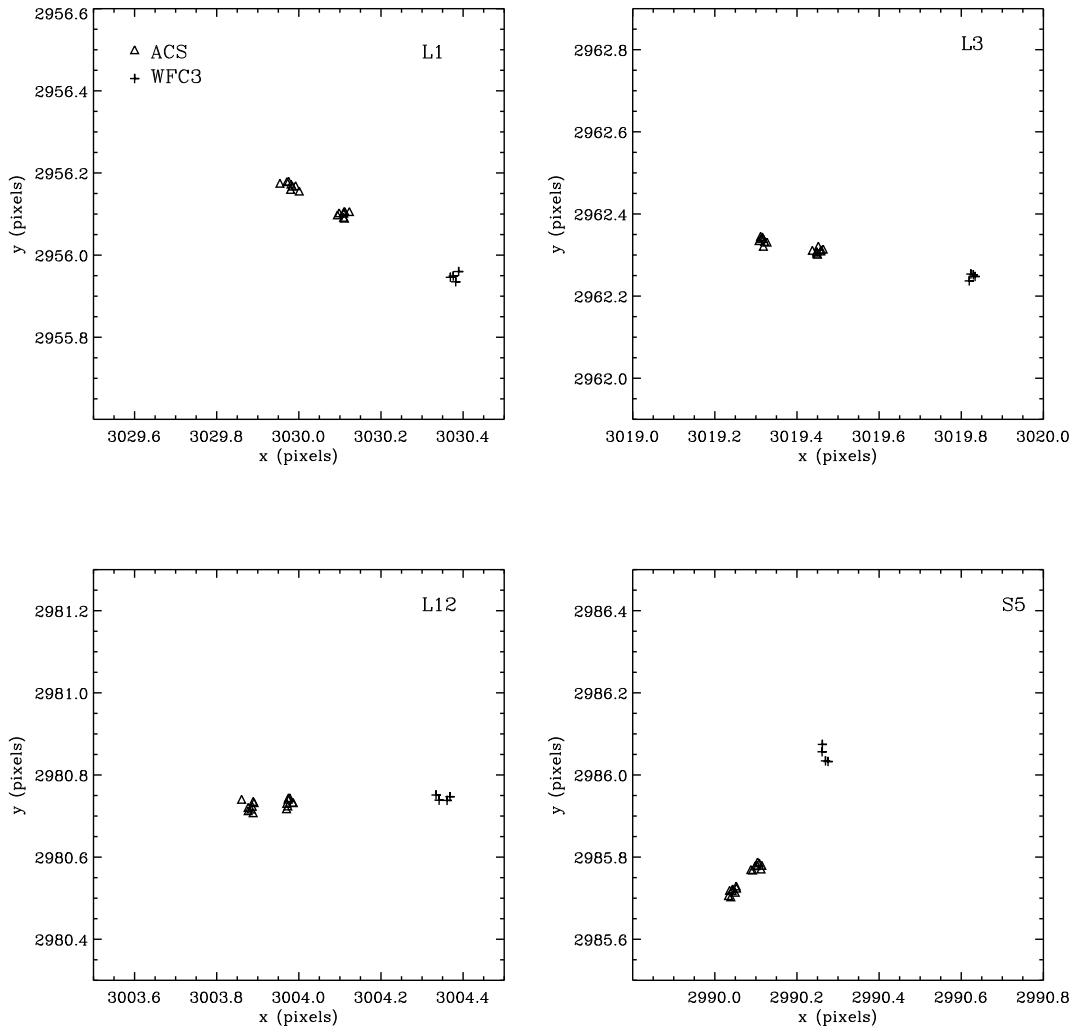


**Figure 4.** The  $x$  vs.  $y$  (equivalent to  $W, N$ ) positions in pixels of the QSO, after transformation into the masterframe, for 4 randomly chosen QSO fields for all 3 epochs of data. The fields are labeled according to Table 1. Linear motion (reflex motion of the L/SMC) is clearly visible, as is the high  $S/N$  consistency across the three epochs. Each symbol represents 1 of the 20 positions of the QSO relative to the starfield, and are distinguished here using triangles for ACS data and plus signs for WFC3 data. The uncertainty in centering the QSO within a given epoch is visible as scatter between the points. The first two ACS epochs are the ones that are most closely spaced in time (and QSO position). The QSO's reflex motion is predominantly towards the West, because the Magellanic Clouds move predominantly towards the East. Each panel is  $1 \times 1$  pixel. 1 pixel = 25 mas.

agrees with the brightest part of the LMC bar. The use of a new rotation center affects the inferred PM of the LMC COM,  $(\mu_{W,LMC}, \mu_{N,LMC})$ , as discussed in Section 4.1.

In Table 1 we list for each field the estimate for the LMC COM that is obtained after subtraction of the contributions from viewing perspective and LMC rotation indicated by the best fit model. In Figure 6 (*bottom*) we show the estimates  $PM_{\text{est}}(\text{COM})$  resulting from this procedure. The scatter is considerably reduced with respect to the top panel. The weighted average of the estimates is  $\mu_{W,LMC} = -1.910 \pm 0.008$  mas yr $^{-1}$  and  $\mu_{N,LMC} = 0.229 \pm 0.008$  mas yr $^{-1}$ . The error bars on these values reflect only the propagation of the random errors in the data. We show in Paper II that there are also contributions from two other sources. First, there is excess scatter between measurements from different fields that is not accounted for by random errors, disk ro-

tation, and viewing perspective. The best-fitting model has a reduced  $(\chi^2_{\text{min}}/N_{\text{DOF}})^{1/2} = 1.8$ ; here  $\chi^2_{\text{min}}$  is the  $\chi^2$  value of the best-fit model. Second, there are uncertainties in the geometry and rotation of the best-fitting LMC disk model that need to be propagated. The latter provide the dominant uncertainty in the final result. When these sources of uncertainty are taken into account as described in Paper II, the final estimate of the LMC COM PM becomes  $\mu_{W,LMC} = -1.910 \pm 0.020$  mas yr $^{-1}$  and  $\mu_{N,LMC} = 0.229 \pm 0.047$  mas yr $^{-1}$ .

### 3.3. SMC COM Motion

For the SMC we have PM measurements for only 5 QSO fields, of which only 3 fields have three-epoch data. This sparse coverage cannot provide much insight into the SMC geometry and rotation field. We therefore fit a relatively simple model to the PM data in order to

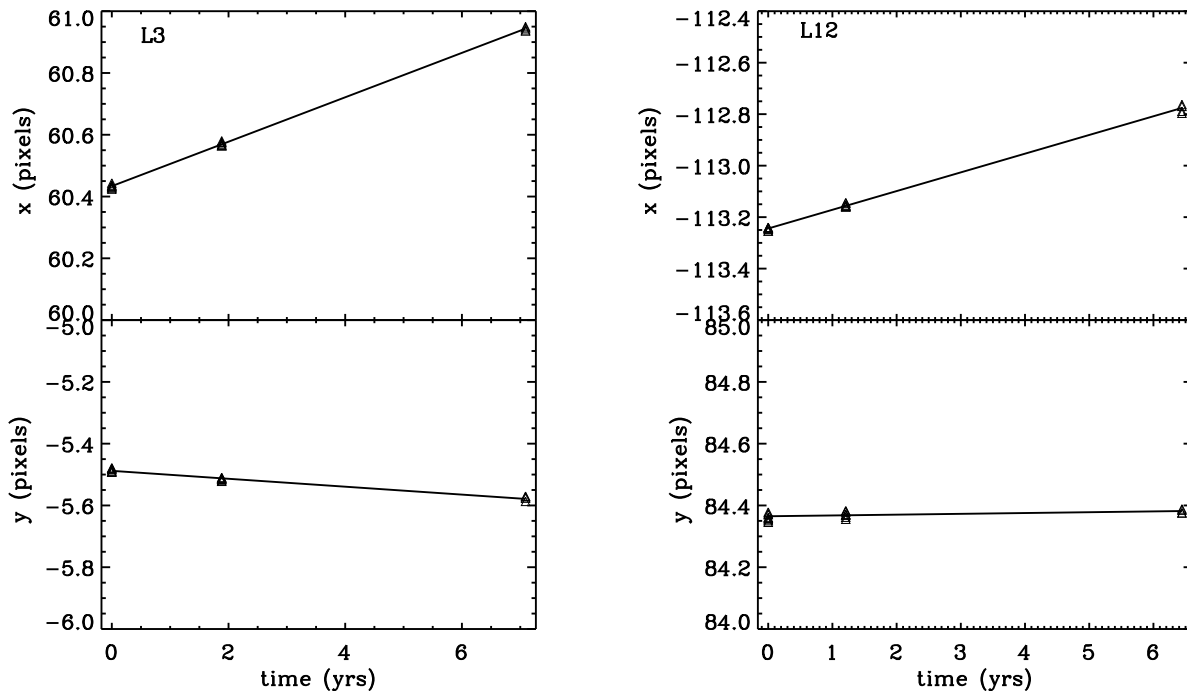


**Figure 5.** Analogous to Figure 4 but now showing  $x$  and  $y$  positions of the QSO in pixels as a function of time for two of the LMC fields also in Figure 4. The fitted linear motion is depicted by the solid lines. 1 pix = 25 mas.

determine the SMC COM PM ( $\mu_{W,SMC}, \mu_{N,SMC}$ ).

To calculate a PM model prediction for each observed field, we keep the SMC center fixed at the H I kinematical center  $(\alpha, \delta) = (16.25^\circ, -72.42^\circ)$  (Stanimirović et al. 2004), the distance modulus fixed at  $m - M = 18.99$  (Cioni et al. 2000), and the radial velocity fixed at  $v_{\text{sys}} = 145.6 \text{ km s}^{-1}$  (Harris & Zaritsky 2006). We account for the influence of viewing perspective as in vdm02. We also allow for the possibility of a single overall rotation of velocity  $V_{\text{rot}}$  in the plane of the sky (i.e., as though we were viewing a face-on disk). We treat the SMC COM PM as a free parameter that is optimized by minimizing the  $\chi^2$  of the model fit to the data.

To determine the uncertainties on the best-fit model parameters, we create pseudo-data in a Monte-Carlo sense from the best-fitting model, with properties similar to the real data. For this we use the observational error bars, but multiplied by a factor  $(\chi^2_{\text{min}}/N_{\text{DOF}})^{1/2}$  to account for the observed scatter between the measurements. Many different pseudo-data sets are created that are analyzed similarly to the real data set. The dispersions in the inferred model parameters are a measure of the  $1\sigma$  random errors on the model parameters. In the Monte-Carlo simulations we also propagate the uncertainties on the model parameters that are kept fixed. We use  $\Delta(m - M) = 0.10$ ,  $\Delta v_{\text{sys}} = 0.6 \text{ km s}^{-1}$ , and an uncertainty of  $0.2^\circ$  per coordinate in the plane of the sky on the SMC center position.

LOS velocity studies provide some insight into the importance of rotation in the SMC. The old stellar population of the SMC, traced by red giants, is consistent with a pressure-supported ( $V < \sigma$ ) spheroidal system

with little evidence for rotation ( $V_{\text{rot}} < 17 \text{ km s}^{-1}$ ; Harris & Zaritsky 2006). This is consistent with the fact that many studies have found a large LOS depth in the SMC (e.g., Crowl et al. (2001)). By contrast the H I gas in the SMC shows rotation with an amplitude of  $\sim 40 \text{ km s}^{-1}$  (Stanimirović et al. 2004). This presumably indicates that the H I gas resides in a more disk-like distribution than the old stars. Young stars (spectral types O, B, A) show evidence for a rotation velocity gradient of similar magnitude as the H I gas, but surprisingly, with a different major axis position angle (Evans & Howarth 2008).

The results of Harris & Zaritsky (2006) suggest that it is reasonable to assume that the SMC has limited rotation in the plane of the sky. If we analyze the PM data with fixed  $V_{\text{rot}} = 0$ , the inferred SMC COM PM is  $\mu_{W,LMC} = -0.772 \pm 0.033 \text{ mas yr}^{-1}$  and  $\mu_{N,LMC} = -1.117 \pm 0.043 \text{ mas yr}^{-1}$ . This can be compared to the result of just taking the weighted average of the 5 SMC PM data-points, which yields  $\mu_{W,LMC} = -0.754 \pm 0.013 \text{ mas yr}^{-1}$  and  $\mu_{N,LMC} = -1.133 \pm 0.016 \text{ mas yr}^{-1}$ . These results are statistically consistent, despite the fact that the weighted average doesn't account for the influence of viewing perspective. In Table 2 we list the estimate for the SMC COM that is obtained after subtraction of the contribution from viewing perspective for each field. Taking the weighted average of results for individual fields yields artificially low error bars, because it doesn't account for the actual scatter between measurements for different fields, or for uncertainties in the geometry and rotation of the SMC.

To assess the importance of rotation, we have also per-

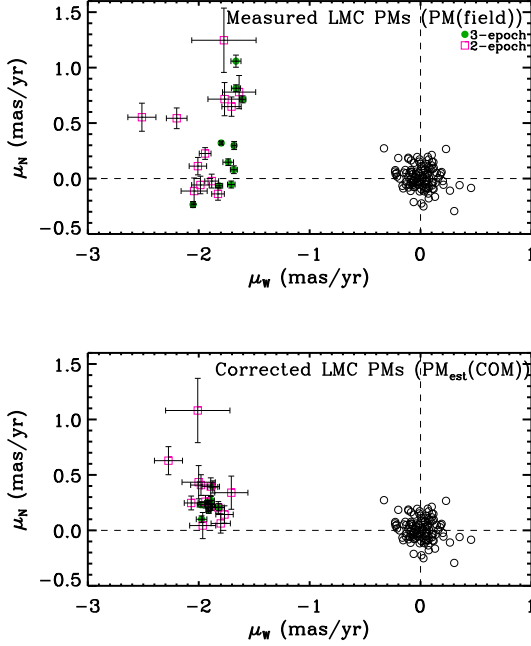


**Figure 6.** (*Top*) PMs for the QSO fields in the LMC (colored symbols) in the  $(\mu_W, \mu_N)$ -plane, compared to the relative star PMs within the fields (open circles; centered around zero by construction). The green filled circles show the results from linear fits to all three epochs of data and the pink squares show results from § 2.3 for e1 and e2 only. (*Bottom*) The estimates  $PM_{est}(COM)$  after subtraction of the field-dependent contributions from viewing perspective and internal motions in the LMC determined in Paper II.

formed model fits in which the rotation is treated as a free parameter to be determined from the PM measurements. This yields  $V_{rot} = 29.5 \pm 24.3 \text{ km s}^{-1}$ . The PM data are therefore reasonably consistent with the absence of rotation, but they don’t provide a very useful constraint. The corresponding best-fit SMC COM PM estimate is  $\mu_{W,LMC} = -0.694 \pm 0.074 \text{ mas yr}^{-1}$  and  $\mu_{N,LMC} = -1.055 \pm 0.078 \text{ mas yr}^{-1}$ . This is consistent with the estimate obtained assuming  $V_{rot} = 0 \text{ km s}^{-1}$ . However, the uncertainties are now significantly increased, due to the allowed variations in the rotation model corresponding to an amplitude variation  $\Delta V_{rot} = 24.3 \text{ km s}^{-1}$ .

As our final SMC COM PM estimate we adopt the result for  $V_{rot} = 0 \text{ km s}^{-1}$ , but allowing for a  $1\sigma$  Gaussian uncertainty  $\Delta V_{rot}$ . Based on the preceding discussion, the average star used in our PM analysis probably rotates significantly less than the H I. We therefore adopt somewhat arbitrarily  $\Delta V_{rot} = 15 \text{ km s}^{-1}$ . This yields for the SMC COM PM that  $\mu_{W,LMC} = -0.772 \pm 0.063 \text{ mas yr}^{-1}$  and  $\mu_{N,LMC} = -1.117 \pm 0.061 \text{ mas yr}^{-1}$ . The uncertainties are almost twice those quoted above, obtained with  $\Delta V_{rot} = 0 \text{ km s}^{-1}$ . So as for the LMC, the quality of the data is now such that the uncertainties in the structure of the Cloud play an important role in how well we can establish the COM PM.

The value of  $(\chi_{min}^2/N_{DOF})^{1/2}$  for the best-fit SMC model is  $\sim 2.8$ , independent of whether  $V_{rot}$  is treated as a free parameter or not. By contrast, for the best-fit LMC model derived in Paper II,  $(\chi_{min}^2/N_{DOF})^{1/2} = 1.8$ .

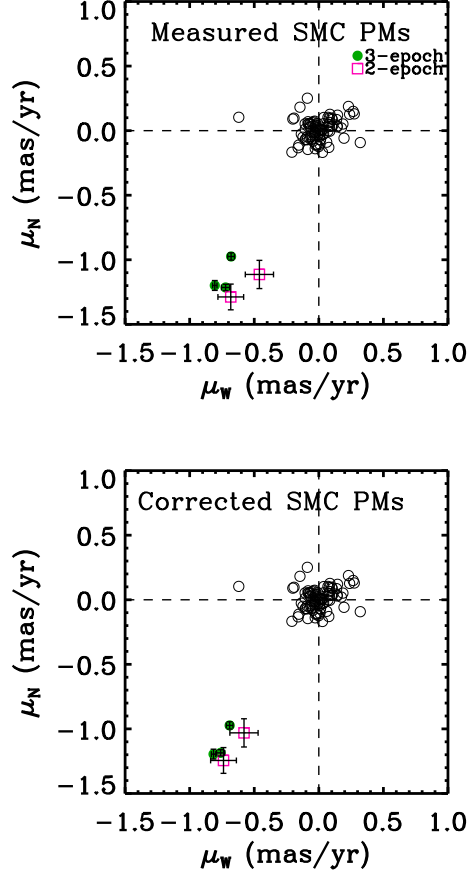


**Figure 7.** (*Top*) Measured QSO motions (colored symbols) with respect to stellar motions (open circles), similar to Figure 6, but now for the SMC. Green filled circles show results from all three epochs of data, and the pink squares for e1 and e2 only. The bottom panel assumes  $V_{rot} = 0 \text{ km s}^{-1}$ .

Therefore, for both galaxies the measurements show somewhat more scatter than what can be accounted for by the models. This is not surprising, given the complexity of the data analysis, and the relatively idealized nature of the models. Additional scatter might be due, e.g., to subtle detector geometric distortion variations over time, residual astrometric effects due to imperfect CTE, or more complicated galaxy structures than are accounted for in the models. It is intriguing that  $(\chi_{min}^2/N_{DOF})^{1/2}$  is larger for the SMC than for the LMC. This might indicate that the structure and kinematics of the SMC are more complex (or less in dynamical equilibrium) than that of the LMC.

#### 4. COMPARISON TO PREVIOUS PM RESULTS

##### 4.1. Previous HST Results

PM measurements from various sources, including the present paper, are summarized in Table 4. For the LMC, K1 obtained from two-epochs of data that  $\mu_{W,LMC} = -2.03 \pm 0.08 \text{ mas yr}^{-1}$  and  $\mu_{N,LMC} = 0.44 \pm 0.05 \text{ mas yr}^{-1}$ . P08 obtained from the same data that  $\mu_{W,LMC} = -1.956 \pm 0.036 \text{ mas yr}^{-1}$  and  $\mu_{N,LMC} = 0.435 \pm 0.036 \text{ mas yr}^{-1}$ . If we analyze the new PM data with the same *fixed* LMC center, inclination angle, and

line-of-nodes position angle from vdM02 used by K1 and P08, we obtain  $\mu_{W,LMC} = -1.899 \pm 0.017 \text{ mas yr}^{-1}$  and  $\mu_{N,LMC} = 0.416 \pm 0.017 \text{ mas yr}^{-1}$ . This shows that the addition of our new third epoch of data, while keeping the LMC model the same, has the following effects: (a) the random errors in the final LMC COM PM components decrease, as expected based on the increased time baseline for about half the fields; (b) the value of  $\mu_{W,LMC}$  decreases by about  $1.6\sigma$  compared to the earlier estimates; and (c) the value of  $\mu_{N,LMC}$  remains unchanged compared to the earlier estimates, within the uncertainties.

Despite this good consistency, our final LMC result of  $\mu_{W,LMC} = -1.910 \pm 0.020 \text{ mas yr}^{-1}$  and  $\mu_{N,LMC} = 0.229 \pm 0.047 \text{ mas yr}^{-1}$  deviates significantly from the final K1 and P08 estimates. This is because of the different LMC model used here, and in particular, the different position for the center. The difference is primarily evident as a decrease by  $\sim 0.20 \text{ mas yr}^{-1}$  in  $\mu_{N,LMC}$ . By contrast, our new value for  $\mu_{W,LMC}$  agrees with that of P08 at the  $1.1\sigma$  level. It is also worth noting that our final best-fit estimate does not have uncertainties that are much lower than those of P08, in particular in  $\mu_{N,LMC}$ . However, the reason for this is that P08 and K1 underestimated the uncertainties, by not propagating all relevant uncertainties in the LMC disk model. Therefore, our new values are in fact significantly more accurate (both in a random and systematic sense) than the older ones.

For the SMC, our results are more similar to those of P08 than K2. This is due primarily to the way in which we combined the results for different fields in K2. On a field-by-field basis, K2 and P08 actually obtained rather similar results. In K2 we didn't explicitly correct for the astrometric effects of CTE. So we reported a value that was essentially an average of only 2 fields, because 3 of the 4 used QSO fields had been taken with the same roll angle at both epochs. We also increased our errors to reflect a 'true' systematic plus random error, estimated from our analysis of the more numerous LMC fields. The K2 result therefore had large errorbars. While our new three-epoch result agrees with K2 for  $\mu_{N,SMC}$ , for  $\mu_{W,SMC}$  it differs by  $2.4\sigma$ . Again, this is mainly because of the way in which fields were combined in K2. The new three-epoch result, however, includes CTE corrections and a longer time baseline, and is therefore the more accurate one.

Our three-epoch result for the SMC agrees reasonably well with that of P08. The value for  $\mu_{W,SMC}$  agree within the uncertainties, while for  $\mu_{N,SMC}$  the results differ by  $1.7\sigma$ . This agreement is similar as for the LMC, if one compares analyses with the same assumed LMC center. So overall, there is acceptable internal consistency between studies with different analysis methods, scientific instruments, and time baselines.

#### 4.2. Ground-based Results

A number of older ground-based (and Hipparcos) analyses of the LMC and SMC PMs were discussed in K1 and K2. These studies had large uncertainties, but within these uncertainties the results were generally consistent with what we know now from *HST* data.

There are now more recent results from two groups that are worth discussing (see Table 4). Vieira et al. (2010)

measured the PMs of the Clouds based on CCD and plate material from the Yale/San Juan Southern Proper Motion program, spanning a baseline of 40 years, and covering a large area in the inter-Cloud region as well. They ultimately tie their reference frame to the ICRS. Within the uncertainties of  $\sim 0.3 \text{ mas yr}^{-1}$  per coordinate, their LMC and SMC PM determinations agree with those presented here. They obtain a stronger constraint on the relative motion between the Clouds, than on the motion of either cloud individually:  $(\mu_W, \mu_N)_{SMC-LMC} = (0.91, -1.49) \pm (0.16, 0.15) \text{ mas yr}^{-1}$ . The corresponding difference between the Clouds' motions from our new *HST* results is:  $(\mu_W, \mu_N)_{SMC-LMC} = (1.188, -1.383) \pm (0.039, 0.064) \text{ mas yr}^{-1}$ . These results agree for  $\mu_N$ , but differ by  $1.7\sigma$  for  $\mu_W$ . Given the totally different methodologies, this is a satisfactory result. However, the uncertainties on the ground-based data are large enough that they don't really help to validate the *HST* data at the level of its own uncertainties.

Costa et al. performed two recent studies using the 2.5m telescope at Las Campanas and centered on background QSOs. In Costa et al. (2009) they measure 1 fairly outlying QSO in the LMC over a 5 year baseline. The inferred LMC COM PM depends significantly on the assumed LMC rotation velocity. In Table 4 we quote the average of their results for  $V_{\text{rot}} = 50 \text{ km s}^{-1}$  and  $120 \text{ km s}^{-1}$  (which corresponds to a rotation velocity consistent with that derived in Olsen et al. (2011) and Paper II). The uncertainties are  $0.13\text{--}0.15 \text{ mas yr}^{-1}$  per coordinate. Their PM value differs from our new *HST* result by  $1.5\sigma$  in  $\mu_{W,LMC}$  and  $1.8\sigma$  in  $\mu_{N,LMC}$ . This is more than expected based on random errors alone. However, we are unable to evaluate our *HST* results on the basis of this study, given that we have many more quasars and typically higher accuracy.

Costa et al. (2011) present an SMC COM PM estimate from 5 QSO fields over a 7 year baseline. This is similar to our study, but *HST* of course has better spatial resolution. Their PM value differs from our new *HST* result by  $1.5\sigma$  in  $\mu_{W,LMC}$ , but agrees in  $\mu_{N,LMC}$  to within the uncertainties. Given the totally different methodologies compared to our work, this too is a satisfactory result. However, again the uncertainties on the ground-based data are large enough that they don't really help to validate the *HST* data at the level of its own uncertainties.

#### 5. GALACTOCENTRIC VELOCITIES

The methodology for transforming an observed PM to a space motion in the Galactocentric rest frame is described in vdM02. The correction for the solar reflex motion requires knowledge of the Solar motion in the Milky Way. In K1 and K2 we adopted the standard IAU value (Kerr & Lynden-Bell 1986) for the circular velocity of the Local Standard of Rest (LSR),  $V_0 = 220 \text{ km s}^{-1}$ . However, models based on the PM of Sgr A\* (Reid & Brunthaler 2004) and masers in high-mass star-formation regions (Reid et al. 2009) have suggested that the circular velocity may be higher. Shattow & Loeb (2009) argued that this may significantly affect the orbit of the Magellanic Clouds. McMillan (2011) has presented a Milky Way analysis that includes all relevant observational constraints, from which he derived  $V_0 = 239 \pm 5 \text{ km s}^{-1}$ . This is the value that we will adopt for the present study. We

also use the McMillan (2011) value for the distance of the Sun from the Milky Way,  $R_0 = 8.29 \pm 0.16$  kpc. For the peculiar velocity of the Sun with respect to the LSR we adopt the recent estimate from Schönrich et al. (2010):  $(U_{\text{pec}}, V_{\text{pec}}, W_{\text{pec}}) = (11.1, 12.24, 7.25)$ , with uncertainties of  $(1.23, 2.05, 0.62)$  km s $^{-1}$  (being the quadrature sum of the random and systematic errors). Previous work adopted the solar peculiar velocity from Dehnen & Binney (1998). However, there is now increasing evidence that  $V_{\text{pec}}$  from that study is too small by  $\sim 7$  km s $^{-1}$ . As a result, the solar velocity in the Galactocentric  $Y$ -direction,  $v_Y = V_0 + V_{\text{pec}}$ , is 251.2 km s $^{-1}$  in our calculations here (consistent with the recent Bovy et al. (2012) study who find  $v_Y = 242_{-3}^{+10}$  km s $^{-1}$ ). By contrast, it was 26 km s $^{-1}$  lower in the calculations of K1 and K2. This directly impacts the LMC and SMC space velocity.

In Table 5 we list the space velocity in the Galactocentric rest frame of both the LMC (lines 1–6) and SMC (lines 7–10), implied by the various PM measurements available from *HST*. We also list the corresponding relative velocity of the SMC with respect to the LMC (lines 11–14). The relative velocity does not depend on the assumed solar motion. However, the individual LMC and SMC velocities do depend on the solar motion. For all PM measurements we list (labeled “IAU”) the results obtained under the assumption of the IAU value of  $V_0 = 220$  km s $^{-1}$  and the Dehnen & Binney (1998) solar peculiar velocity. For the new three-epoch measurements from the present paper we list also the results (labeled “new”) obtained under the assumption of the McMillan (2011) value of  $V_0 = 239 \pm 5$  km s $^{-1}$  and the Schönrich et al. (2010) solar peculiar velocity. For all results we assume a distance uncertainty  $\Delta m - M = 0.1$  mag. For the IAU value of  $V_0$  we also (arbitrarily) set the uncertainty to be  $\Delta V_0 = 5$  km s $^{-1}$ ; the actual uncertainty must be significantly larger, if the McMillan (2011) results are indeed correct. The space motions that we derive based on the K1, K2 and P08 PMs, with the “IAU” solar motion, are consistent with the values quoted in those papers. However, our errorbars are generally larger and more accurate. This is because these previous studies did not propagate the error in distance, which is in fact a dominant error term (since  $v \propto D\mu$ ).

The final results from the present paper are presented in lines 1, 7, and 11 of Table 5. This uses the three-epoch PM dataset. For the LMC, it uses the LMC geometry and rotation determined from the PMs in Paper II. The results are characterized by the following properties. The LMC has a total velocity (i.e., length of the Galactocentric velocity vector) of  $v_{\text{tot,LMC}} = 321 \pm 24$  km s $^{-1}$ . The SMC has a total velocity  $v_{\text{tot,SMC}} = 217 \pm 26$  km s $^{-1}$ . For both galaxies, the radial velocity  $v_{\text{rad}}$  is much less than the tangential velocity  $v_{\text{tan}}$ . The value of  $v_{\text{rad,LMC}} > 0$ , so that the Clouds are past pericenter and moving towards apocenter. The relative velocity of the SMC with respect to the LMC is  $v_{\text{tot,rel}} = 128 \pm 32$  km s $^{-1}$ . The radial component of the relative velocity is almost twice the tangential component of the relative velocity. This implies a rather elliptical orbit, but a purely radial orbit ( $v_{\text{tan,rel}} = 0$ ) is ruled out. The value of  $v_{\text{rad,rel}} > 0$ , so that the SMC is past its pericenter with respect to the

LMC, and moving towards apocenter.

The motions derived by K1, K2, and P08 have been used for various studies in recent years. It is therefore of interest to examine how the new results differ from the old results, and why.

**Influence of solar velocity:** Comparison of lines 2 and 1 in Table 5 for the LMC, and lines 8 and 7 for the SMC, shows that going from the old to the new values for the solar velocity decreases all of  $v_{\text{tot}}$ ,  $v_{\text{rad}}$  and  $v_{\text{tan}}$ , by 15–22 km s $^{-1}$ . This is consistent with arguments made by Shattow & Loeb (2009) about the influence of the solar velocity on the computation of the Clouds’ orbits.

**Influence of LMC center position:** Comparison of lines 3 and 1 shows that going from the vdM02 center (consistent with the center of the LMC bar) to the new LMC center from Paper II (consistent with the H I dynamical center), reduces  $v_{\text{tot}}$ ,  $v_{\text{rad}}$  and  $v_{\text{tan}}$  only minimally ( $\sim 7$  km s $^{-1}$ ). However,  $\mu_{N,LMC}$  decreases by  $\sim 0.2$  mas yr $^{-1}$  (see Table 4) which equals  $\sim 47$  km s $^{-1}$ . This therefore changes primarily the angle of the tangential velocity as seen in projection from the Galactic Center, as previously pointed out by B07. The change is such so as to better align the past orbit with the location of the Magellanic Stream, but not to fully align it as we will discuss in §6.

**Influence of third-epoch data for the LMC:** Comparison of lines 6, 5 and 4 shows that (when using the same solar velocity and the same parameters for the LMC geometry from vdM02) the addition of the third epoch WFC3 data and the reanalysis of the two-epoch ACS data decreases  $v_{\text{tot}}$  and  $v_{\text{tan}}$  for the LMC by  $\sim 30$  km s $^{-1}$ , when going chronologically from K1, to P08, to the present paper. These changes are due to a progressive decrease in  $|\mu_{W,LMC}|$ . The value of  $v_{\text{rad}}$  stays more-or-less the same.

**Influence of third-epoch data for the SMC:** Comparison of lines 10, 9 and 8 shows that (when using the same solar velocity) the addition of the third epoch WFC3 data and the reanalysis of the two-epoch ACS data decreases  $v_{\text{tot}}$  and  $v_{\text{tan}}$  for the SMC by  $\sim 65$  km s $^{-1}$  (a  $\sim 1\sigma$  change from the K2 velocities and errors), when going chronologically from K2, to P08, to the present paper. These changes are due to how the K2 data from different fields were combined, which leads to a large difference in the inferred  $\mu_W$  component compared to what is obtained from a simple average of all the fields. The K2 combination strategy also increased the error bars, however, which is why there is consistency at the  $1\sigma$  level. The new data also indicate a small decrease in  $|\mu_{N,SMC}|$  compared to P08. The value of  $v_{\text{rad}}$  changes by less than  $\sim 15$  km s $^{-1}$ .

**Influence of third-epoch data on velocity uncertainties:** Comparison of lines 6, 5, and 4, or 10, 9, and 8, respectively, does not show much of a decrease in random errors on the velocities, when going chronologically from K1/K2, to P08, to the present paper. This is because the PMs are now accurate enough that much of the velocity uncertainty is driven by distance uncertainties. These distance uncertainties were ignored in these previous papers, producing overly optimistic error bars.

Many of these individual influences change the Galactocentric velocities in a similar direction. As a result, our

new velocities are quite different from those found by K1 & K2.

**New LMC velocity compared to K1:** Our new velocity has lower  $v_{\text{tot}}$  and  $v_{\text{tan}}$  by  $\sim 57 \text{ km s}^{-1}$ . This is due to a combination of two effects: a  $\sim 30 \text{ km s}^{-1}$  decrease due to a lower value of  $|\mu_{W,LMC}|$  and a  $\sim 27 \text{ km s}^{-1}$  decrease due to a revised understanding of the solar velocity. The latter also decreases  $v_{\text{rad}}$  by  $\sim 25 \text{ km s}^{-1}$ . Moreover, we also derive a lower value of  $|\mu_{N,LMC}|$  due to a change in the derived LMC center. The new  $v_{\text{tot}}$  is approximately halfway between the traditional orbit required by tidal Magellanic Stream models in a logarithmic halo (Gardiner & Noguchi 1996, hereafter GN96), and the K1 result that led B07 to suggest using  $\Lambda$ CDM-motivated halo models that the Clouds may be on their first passage about the MW. We therefore perform new orbit calculations in §6.

**New SMC velocity compared to K2:** Our new velocity has lower  $v_{\text{tot}}$  and  $v_{\text{tan}}$  by  $\sim 85 \text{ km s}^{-1}$ . This is due to a combination of two effects: a  $\sim 65 \text{ km s}^{-1}$  decrease due to a lower value of  $|\mu_{W,SMC}|$  (mainly due to how the fields were combined in K2) and a  $\sim 20 \text{ km s}^{-1}$  decrease to a revised understanding of the solar velocity. The latter is also primarily responsible for decreasing  $v_{\text{rad}}$  by  $\sim 34 \text{ km s}^{-1}$ . There is also a smaller contribution from the different SMC center used here compared to K2.

**New relative SMC-LMC velocity compared to K2:** The total relative velocity  $v_{\text{tot}}$  has changed very little. However,  $v_{\text{rad}}$  is now larger than  $v_{\text{tan}}$ , so the orbit is more elliptical than before. The value of  $v_{\text{tot}}$  is not quite as high as found by P08, but consistent within the errors.

## 6. ORBIT IMPLICATIONS

The PMs and Galactocentric velocities from K1 & K2 have been used in many studies to look at the past orbit of the Magellanic Clouds with respect to the MW, and the formation of the Magellanic Stream. As discussed in the preceding sections, the latest *HST* observations and data analysis, combined with the latest understanding of the LMC geometry and solar velocity, imply decreased Galactocentric velocities, and improved understanding of the observational errors. We therefore rederive here the past orbit of the Magellanic Clouds based on the new results.

### 6.1. Methodology and Parameter Space

We explore a total of 5 models for the MW: 3 static models with total virial masses of  $10^{12}$ ,  $1.5 \times 10^{12}$ , and  $2 \times 10^{12} M_{\odot}$ ; and two cases in which we allow for the mass evolution of the MW as is expected from the hierarchical build up of mass in  $\Lambda$ CDM. While it is beyond the scope of this work to provide an exhaustive compilation of the observational determinations of MW mass, we do want to motivate our adopted range by pointing to the work of Gnedin et al. (2010), who obtain a MW virial mass of  $1.6 \times 10^{12} M_{\odot}$  if the middle value for their data-based circular velocity determination is used. The uncertainty around this value is 20%.

For the static MW cases we follow B07 and model the MW as an axisymmetric three-component potential with a NFW halo, Miyamoto-Nagai disk (Miyamoto & Nagai 1975) and a Hernquist bulge (Hernquist 1990). In all

cases the bulge is modeled with a scale radius of 0.7 kpc and total mass of  $10^{10} M_{\odot}$ . The NFW halo is adiabatically contracted to account for the presence of the disk using the CONTRA code (Gnedin et al. 2004). The NFW density profile is also truncated at the virial radius (unlike in B07). While it is widely agreed that halos should be truncated, exactly how and where the truncation is done is arbitrary. The exact nature of this truncation does not affect our conclusions, because we consider a one-parameter family of models in which MW halo mass is considered a free parameter.

Halo and disk parameters are listed in Table 6. In all cases the disk scale radius is kept fixed at 3.5 kpc while the total disk mass is allowed to vary in order to reproduce the correct circular velocity at the solar circle. The MW circular velocity is taken as the updated value of  $239 \text{ km s}^{-1}$  at the solar radius of 8.29 kpc (McMillan 2011), rather than the standard IAU value, in all models, unlike B07. Rotation curves for each MW model are presented in Figure 8. We follow the methodology outlined in B07 to capture the effects of dynamical friction acting on the Clouds owing to their passage through the MW’s dark matter halo.

In the cases where the LMC is not on a first passage but has had a past pericentric passage, the typical periods are quite large ( $\gtrsim 5 \text{ Gyr}$ ). As such, we also want to investigate a simple model that accounts for the MW’s mass evolution over the past 10 Gyr. In this case we model the MW only as a NFW halo (neglecting the disk, etc.). We model the mass evolution following the mean mass growth rate with redshift from Fakhouri et al. (2010). The expected  $1\sigma$  scatter in this evolution at each redshift is roughly 20% (from Figure 1 of Boylan-Kolchin et al. 2010). We model the concentration evolution following Klypin et al. (2011), and the scaling of the virial radius with redshift and mass following relations in Maller & Bullock (2004)<sup>7</sup>. We consider current-day MW virial masses of  $1.5 \times 10^{12} M_{\odot}$  and  $2 \times 10^{12} M_{\odot}$  in this exercise. We only explore the higher MW mass range because we are interested in constraining whether the LMC is on a first infall (and as we will show below, it is always on a first infall in the low MW mass case).

Our expectation is that the LMC mass is the dominant uncertainty in its orbital history (over MW mass evolution), since dynamical friction will change the LMC’s orbit on timescales shorter than the MW’s mass evolution<sup>8</sup>. Therefore, for each static MW mass model, a variety of LMC masses are explored, ranging from  $3 \times 10^{10}$  to  $2.5 \times 10^{11} M_{\odot}$  (the motivation for which is discussed directly below). This approach is different from B07, where we only considered one LMC mass of  $3 \times 10^{10} M_{\odot}$ .

Our knowledge of the mass of the LMC is limited by the fact that kinematic data are only available in the inner

<sup>7</sup> The Fakhouri et al. (2010) work is based on the Millenium II simulations and therefore uses an old value for  $\sigma_8$ , while the Klypin et al. (2011) work uses the Bolshoi simulations which have an updated value for  $\sigma_8$ . However, we do not think that this inconsistency should affect MW mass objects very much, since the old value of  $\sigma_8$  primarily suppresses power on low-mass scales.

<sup>8</sup> However, the MW’s mass evolution can substantially modify solutions with orbital periods of order  $\gtrsim 6 \text{ Gyr}$ , as the Fakhouri et al. (2010) relations imply that the MW’s halo should be  $\sim 65\%$  as massive 6 Gyr ago (see also Moster et al. 2012).

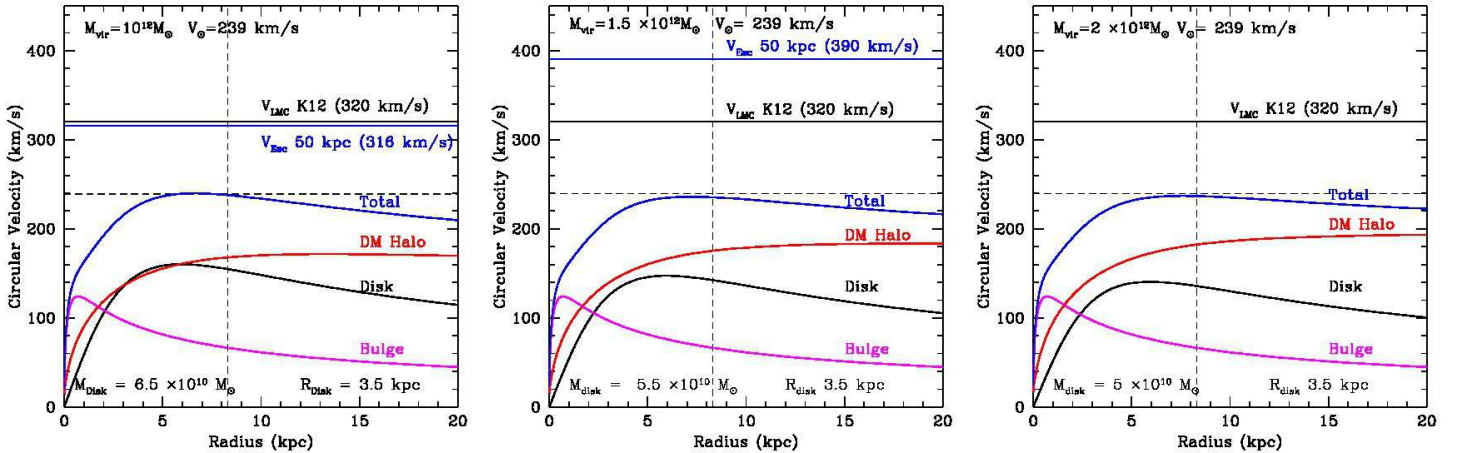


**Figure 8.** Rotation curves for the three static MW potentials that we explore, with MW virial mass =  $1 \times 10^{12} M_{\odot}$  (left),  $1.5 \times 10^{12} M_{\odot}$  (middle), and  $2 \times 10^{12} M_{\odot}$  (right).  $V_{\odot}$ , the Sun’s velocity at the solar circle, is  $239 \text{ km s}^{-1}$  in all three cases, as indicated by the horizontal dashed line in each panel.  $R_{\odot}$ , the solar radius, is kept fixed at  $8.29 \text{ kpc}$ , as indicated by the vertical dashed lines. The panels also indicate the amount of mass in the MW disk, as well as its disk scale-length. The horizontal black line shows the mean third-epoch LMC velocity derived here. The horizontal blue line shows the value for the MW escape velocity at  $50 \text{ kpc}$ . In the  $2 \times 10^{12} M_{\odot}$  MW case, the escape velocity =  $435 \text{ km s}^{-1}$  (just outside plotting range).

$\sim 9 \text{ kpc}$ . The observational estimate of LMC total mass within this distance is  $1.3 \times 10^{10} M_{\odot}$  (van der Marel et al. 2009). For each mass case considered here, the LMC is modeled as a Plummer sphere, where the softening radius is chosen such that the total mass contained within  $9 \text{ kpc}$  is  $\sim 1.3 \times 10^{10} M_{\odot}$  as observed, and as listed in Table 6.

Saha et al. (2010) have detected stars out to  $10$  disk scale-lengths in the LMC (at a scale-length of  $1.4 \text{ kpc}$ , this amounts to stars as far out as  $15 \text{ kpc}$ ). For a bound stellar component to exist at a minimum distance of  $15 \text{ kpc}$  from the LMC center-of-mass, the tidal radius must be at least this large. In a  $2 \times 10^{12} M_{\odot}$  MW, the LMC’s Roche radius at a MW-LMC separation distance of  $49.5 \text{ kpc}$  reaches  $15.4 \text{ kpc}$  if the LMC total mass is  $3 \times 10^{10} M_{\odot}$ . This is the reason for our choice of lower bound in LMC mass. The highest total LMC mass explored is chosen to match the observed present-day LMC stellar mass and the relations for the expected infall mass from Guo et al. (2010). For the evolving MW mass case we only consider LMC mass =  $5 \times 10^{10} M_{\odot}$ . For this LMC mass we expect to find solutions where the LMC has completed an orbit about the MW, and this thus serves as a fiducial case for testing the plausibility of a non-first infall scenario.

Whether the SMC is a binary companion to the LMC is primarily determined by the LMC mass, which provides further motivation for varying the LMC mass. If the SMC is a long-term companion of the LMC, it will have been tidally truncated fairly early on, maintaining a roughly constant mass within its tidal radius at late times. Therefore, we do not vary the SMC mass. The SMC is modeled as a Plummer sphere of total mass  $3 \times 10^9 M_{\odot}$ , with a Plummer softening of  $1 \text{ kpc}$  so that the mass within  $3.5 \text{ kpc}$  is  $2.4 \times 10^9 M_{\odot}$  (Stanimirović et al. 2004). We do not account for dynamical friction acting on the SMC as it travels through the dark matter halo of the LMC. This is not significantly different than the approach used in B07.

In our study we use the new 3rd epoch values and updated solar motion for both the LMC and SMC, and their corresponding errors (see lines 1 and 7 of Table 5).

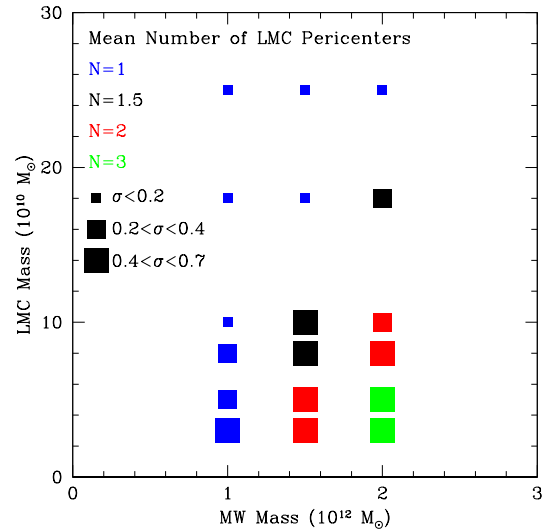


**Figure 9.** The average number of pericentric passages that the LMC has made about the MW, as a function of LMC and MW mass, is indicated by different colors. Note that in all cases the LMC has at least made one pericentric passage since it is just at pericenter now, according to our data ( $N$  always starts at 1). The  $N=1.5$  case represents orbits where there is roughly equal probability that the LMC is on first infall ( $N=1$ ) or has completed one orbit ( $N=2$ ). The point size indicates the RMS errors on the average value, as indicated in the legend by black symbols.

## 6.2. Orbits about the Milky Way

As in B07 we follow the orbit of the LMC backward in time, using the present day velocities and positions and integrating the corresponding equations of motion<sup>9</sup>. For each combination of MW and LMC mass, we explore  $10,000$  Monte-Carlo drawings from the LMC’s velocity error distribution. We calculate the evolution of the LMC’s Galactocentric radius, and keep track of how

<sup>9</sup> We implicitly assume here that the LMC and SMC are a binary, and that therefore the more massive LMC sets the orbital path. We ignore the SMC in this part of the calculation (but see §6.3).

many pericentric passages it makes about the MW over a Hubble time, assuming the MW mass is static over this time period. In Figure 9 we show the mean number of pericentric passages that the LMC has made about the MW, as a function of LMC and MW mass. Note that in all cases the LMC has made at least one pericentric passage ( $N=1$ ): our data indicate that the LMC is currently just past pericenter, in agreement with previous works. This does not, however, imply that the LMC has made a complete orbit about the MW. The combination of LMC and MW masses that yield, on average, solutions where the LMC has completed at least one orbit are indicated by  $N \geq 2$ ; first infall scenarios are indicated by  $N=1$ .  $N=1.5$  represent cases where there is roughly equal probability that the LMC is on a first infall or that it makes one orbit about the MW (50% of the solutions have  $N=1$  and 50% have  $N=2$ ). The size of the square indicates the RMS error on the mean value, as listed in the legend.

For the majority of the cases we consider here, the LMC makes no additional pericentric passages about the MW than the one that it is currently at (it is on a first infall: dark blue squares). As might be expected, the LMC makes more pericentric passages if the MW mass is higher (larger binding energy) and the LMC mass is lower (minimal dynamical friction). The dispersion in the mean values increases as the mass of the MW increases; there are more solutions with one or more complete orbits allowed within the error space within a Hubble time for higher mass MW models. The dispersion decreases as the LMC’s mass increases; for high mass LMC models (consistent with  $\Lambda$ CDM expectations, Guo et al. 2010) dynamical friction limits the number of closed orbit solutions within the error space. This forces the LMC on increasingly eccentric orbits with orbital periods longer than a Hubble time.

Note that we have ignored the mass evolution of the LMC owing to the MW’s tidal field in this analysis. Because we have constrained all LMC models to match the total observed mass of the LMC within 9 kpc, higher mass LMC models will have more material at large radii and should thus be more affected by the omission of this physical effect than the lower mass LMC models. However, Figure 9 illustrates that if the LMC today is well-described by the high mass models, it could not have made an earlier pericentric approach about the MW. As such, our argument is self-consistent.

Figure 9 does illustrate that solutions can be found where the LMC makes more than one complete orbit about the MW within a Hubble time. For these cases, Figure 10 illustrates the mean orbital period for the most recent orbit. Note that if the LMC has completed more than one orbit, the orbital period of the previous passage is expected to be larger than the values quoted for the most recent passage because of dynamical friction. For the  $1 \times 10^{12} M_{\odot}$  MW, the periods are  $> 9$  Gyr. For the  $1.5 \times 10^{12} M_{\odot}$  MW, the typical periods are  $> 5$  Gyr. In the most tightly bound scenario (LMC mass  $= 3 \times 10^{10} M_{\odot}$ , static MW mass  $\sim 2 \times 10^{12} M_{\odot}$ ), the LMC completes on average 2 orbits about the MW where the most recent orbital period is 3-4 Gyr. This conclusion is no different than in B07 where we showed that the high MW model recaptures the isothermal sphere orbit from

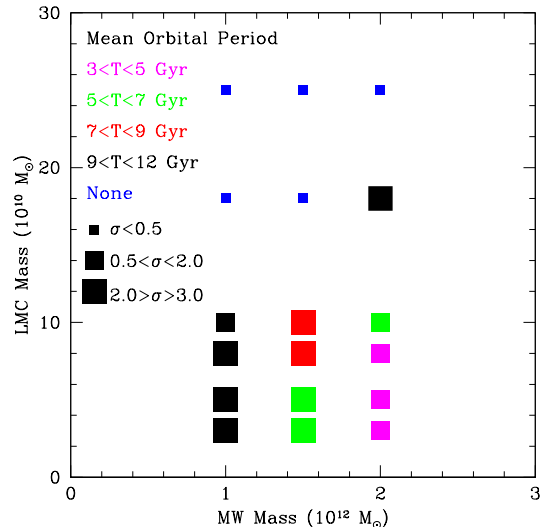


**Figure 10.** The mean period is computed for only those orbits that are closed within a Hubble Time, and is indicated using colors that correspond to duration. For example, if a particular MW-LMC mass combination produces 80% of LMC orbits with  $N=1$ , and 20% with  $N=2$ , then we only plot the average of the 20%. The symbol size indicates the RMS in distribution of periods, as indicated in the legend with black symbols.

previous studies (albeit with larger orbital periods).

For the cases where the LMC makes at least one complete orbit about the MW, i.e. LMC mass  $< 5 \times 10^{10} M_{\odot}$  and MW mass  $> 1.5 \times 10^{12} M_{\odot}$ , we look at the effect of a cosmologically motivated mass growth history for the MW on the orbital history of the LMC. In Figure 11 we show the LMC Galactocentric radius as a function of time in the past ( $t = 0$  corresponds to today) for a current day MW mass of  $1.5 \times 10^{12} M_{\odot}$  (left) and  $2 \times 10^{12} M_{\odot}$  (right), and for LMC mass  $= 5 \times 10^{10} M_{\odot}$  in both cases. In the first case, the period of the orbit is  $> 8$  Gyr for an evolving MW, which is  $\sim 2$  Gyr longer than for a static MW. The LMC goes well outside the virial radius of the MW, i.e., the orbit is dramatically more eccentric than in the static MW case. In the second case, it is shown that a 3 Gyr orbit would still on average increase by 1 Gyr if the mass evolution of the MW is taken into account. The period of the last complete orbit of the LMC about the MW is critical in figuring out the relative importance of MW tides in forming the Stream (discussed further in the next section).

### 6.3. SMC-LMC Orbits and Implications for the Magellanic Stream

We are also interested in re-evaluating the orbit of the Clouds about each other. A chance three-way encounter between the MW, LMC, and SMC at  $z = 0$  has low probability, and therefore we seek to enumerate under what conditions, given the new velocities, the Clouds constitute a binary for a significant fraction of a Hubble time. Also, we have recently put forth a new Magellanic Stream model that relies on the past interactions between the Clouds when they are far from the MW virial radius, rather than on the influence of the MW on the Clouds-system (Besla et al. 2010; Diaz & Bekki 2011). The orbital history of the SMC about the LMC is critical to

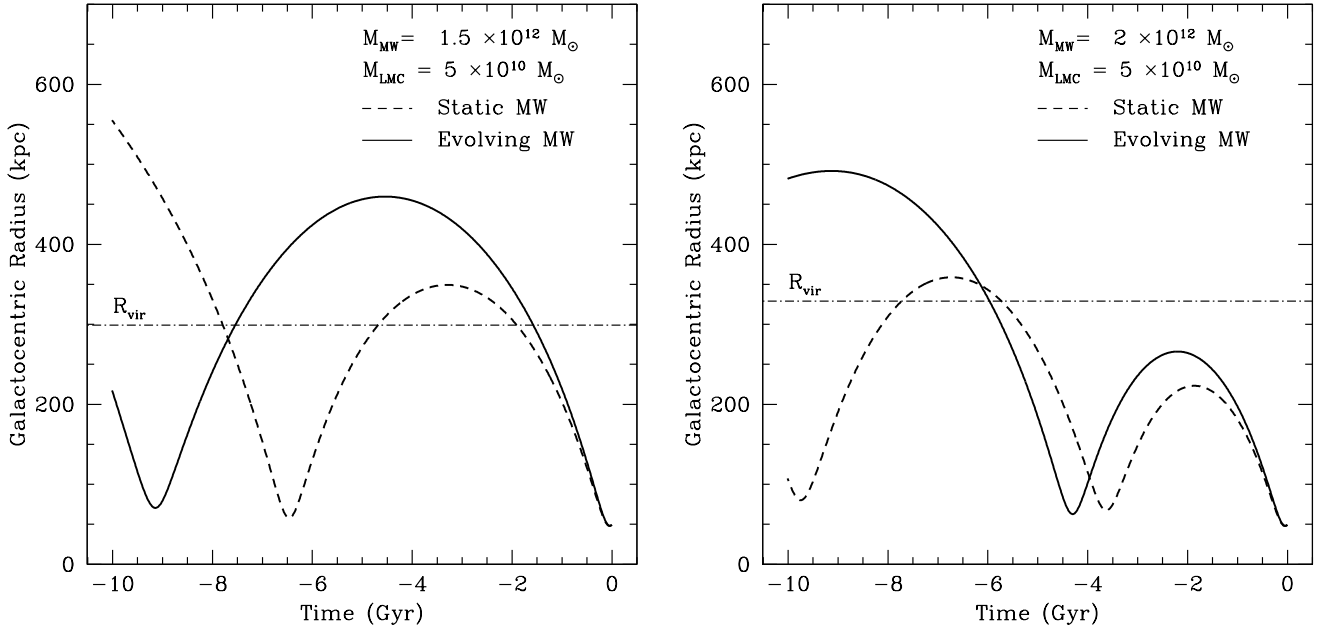


**Figure 11.** *Left:* the LMC Galactocentric radius as a function of time in the past ( $t = 0$  corresponds to today) for a current day MW mass of  $1.5 \times 10^{12} M_{\odot}$  and an LMC mass of  $5 \times 10^{10} M_{\odot}$ . The period of the orbit is  $\sim 2$  Gyr longer for an evolving MW (solid line), and the LMC goes well outside the virial radius of the MW, i.e. the orbit is dramatically more eccentric than in a static MW (dashed line). *Right:* the same for a current day MW mass of  $2 \times 10^{12} M_{\odot}$ . The shortest orbital periods we can obtain are  $\sim 4$  Gyr.

assess the viability of such a model.

We draw 10,000 cases from the LMC and SMC PM error distributions in Monte-Carlo fashion, and orbits are computed for each combination of LMC and MW masses. The SMC is assumed to be tidally truncated and hence its mass is kept fixed at  $3 \times 10^9 M_{\odot}$ . At each time-step, we compute the escape velocity of the SMC from the LMC,  $V_{\text{esc}}$ , and compare this to the relative velocity between the Clouds,  $V_{\text{LS}}$ . We do not require them to be bound today, but rather search for cases at some point in time where  $V_{\text{LS}} < V_{\text{esc}}$ , and keep track of the longest amount of time over which this condition remains true.

This analysis, therefore, accounts for capture events and the fact that the MW’s tidal field might be disrupting the binary today. By also requiring that the escape velocity condition be satisfied, as opposed to searching for minima in the distance between the Clouds as many previous authors have done, we are choosing real binary configurations, rather than chance superpositions caused by cases in which the SMC is on its own elliptical orbit about the MW, and therefore formally gets closer and farther away from the LMC even though the LMC may be on a very different orbit (as illustrated in Růžička et al. 2010).

In *all* searched cases the SMC has made at least one close encounter with the LMC in the past. This is unsurprising, as it is a direct result of the relative orientation of their three-dimensional velocity vectors. The SMC is currently  $\sim 20$  kpc from the LMC and moving away from it. Integrating the SMC’s orbit backwards in time will thus always yield a close encounter with the LMC within the past 500 Myr. This conclusion has been drawn by many previous authors (Růžička et al. 2010, GN96) and is the basis of the LMC-SMC collision theory put forth

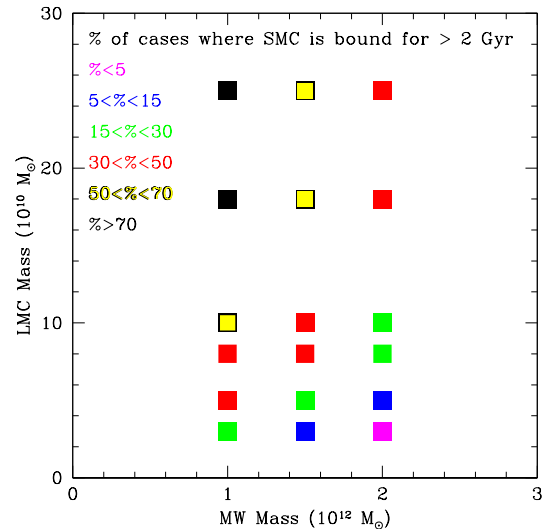


**Figure 12.** The percentage of cases from our 10,000 Monte Carlo drawings in which  $V_{\text{LS}} < V_{\text{esc}}$  for the SMC from the LMC for more than 2 Gyr in the past, shown as a function of LMC and MW mass. The legend shows the color-scheme indicating the range of percentages for each combination of LMC and MW mass.

in Besla et al. (2012).

In Figure 12 we show the outcome of our search for binary orbits between the Clouds. The percentage of Monte Carlo drawings for which  $V_{\text{LS}} < V_{\text{esc}}$  for more than 2 Gyr in the past is shown as a function of LMC and MW mass. We have chosen the 2 Gyr duration since this is the estimated age of the Magellanic Stream (as discussed below), and so the LMC and SMC should be a binary for at least this amount of time in each LMC and MW mass combination. Colored squares indicate the

corresponding percentages, as indicated in the legend.

Unsurprisingly, the percentage of cases for which  $V_{LS} < V_{\text{esc}}$  increases as the mass of the LMC increases (increasing binding energy). However, we also note a dependence on MW mass. At an LMC mass of  $3 \times 10^{10} M_{\odot}$ , the percentage of orbits that satisfies this criterion is 20% if the MW mass is  $1 \times 10^{12} M_{\odot}$ . This number drops to 4% if the MW mass is  $2 \times 10^{12} M_{\odot}$ , implying that bound configurations between the LMC and SMC are statistically unlikely for low LMC mass and high MW mass. As the LMC mass increases, these statistics improve, but for a MW mass of  $2 \times 10^{12} M_{\odot}$ , they only reach 20% once we get to a LMC mass of  $8 \times 10^{10} M_{\odot}$ . The corresponding percentage for a  $1 \times 10^{12} M_{\odot}$  MW is 50%.

The RMS of the distribution of cases matching this escape velocity criteria increases as the LMC mass increases, representing a larger spread in the possible durations. As discussed above, as the MW mass increases there are much fewer binary LMC-SMC orbits, even for high LMC mass. The PMs indicate that the current relative velocity between the Clouds is high. This implies that the SMC must be on an eccentric orbit about the LMC. For larger MW mass models, the tidal field is more effective at disrupting such a wide binary pair.

Therefore, from our statistical analysis we conclude that large LMC masses ( $\gtrsim 1 \times 10^{11} M_{\odot}$ ) are favored if the Clouds are to have been in a binary, and that further, a MW mass  $\lesssim 1.5 \times 10^{12} M_{\odot}$  is also required. From Figure 9, orbits in this mass range almost always correspond to first infall scenarios. The assumption that the Magellanic Clouds constitute a long-lived binary pair thus implies that the Clouds are likely on their first infall about the MW.

Based on our searched parameter space, and the requirement that the LMC and SMC have been a long-lived binary, we adopt a canonical model with the highest MW mass and lowest LMC mass that will fulfill these criteria. This gives (LMC, MW) mass =  $1.8 \times 10^{11} M_{\odot}$ ,  $1.5 \times 10^{12} M_{\odot}$ .

In Figure 13 we show an example of one of these long-lived binary states (N=4–6) in the canonical model (note again that the SMC is assumed to be tidally truncated and therefore kept at fixed mass in our models). The left-hand panel shows the Galactocentric radius of the LMC, the Galactocentric radius of the SMC and the relative distance between the two Clouds as a function of time. The middle panel shows the past orbits of the Clouds in the Galactocentric ( $Y-Z$ )-plane. The right panel shows the past orbit as a function of  $(l, b)$ . Interestingly, the new velocities now cause the past SMC orbit to cross over in the direction of the Stream, something that we did not achieve with the K2 velocities, but was advocated for in earlier works like GN96.

We note that with the vdM02 center, the relative LMC-SMC velocity is  $143 \pm 31 \text{ km s}^{-1}$  (Table 5). With the new center adopted in this work, it is  $128 \pm 32 \text{ km s}^{-1}$ . Since the relative velocity is higher in the former case, the orbit of the SMC would be less bound at fixed mass, and therefore we expected fewer bound cases. Surprisingly, we in fact find *no* binary LMC-SMC orbits when using the vdM02 velocities. We attribute this not just to the larger absolute value of relative velocity, but to the fact that the angle between the velocity vectors is larger. This is an

interesting finding that argues in favor of the new center used here and derived in Paper II.

While dynamical friction owing to the passage of the Clouds through the MW’s dark matter halo was accounted for, we did not explicitly account for dynamical friction acting on the SMC owing to its passage through the LMC’s dark matter halo. The inclusion of this effect would place the SMC on an increasingly eccentric orbit in the past. We have recently advocated for a high eccentricity SMC orbit about the LMC in our simulations of the Magellanic Stream; such eccentric orbits are needed to explain the large angular extent of the Stream and to prevent the Clouds from merging (Besla et al. 2010). However, such eccentric orbits are more easily disrupted by the MW’s tidal field and thus work against maintaining long-lived binary LMC-SMC states. This further strengthens our argument that the preferred mass scale for the MW is less than  $2 \times 10^{12} M_{\odot}$ , since in reality there should be even fewer viable binary orbits in this model than we currently find.

Another way to approach these questions is to look in more detail at the LMC-SMC dynamics in LMC-MW mass combinations that give rise to more traditional orbital trajectories for the Clouds about the MW. Specifically, consider the case of a low-mass (tidally truncated)  $3 \times 10^{10} M_{\odot}$  LMC orbiting around a  $2.0 \times 10^{12} M_{\odot}$  MW, with an orbital period of  $\sim 4$  Gyr. We draw 10,000 LMC and SMC PMs in Monte-Carlo fashion from their error distributions, and plot the relative proper motion between the two Clouds in Figure 14. Each value is color-coded by the length of time for which the criterion  $V_{LS} < V_{\text{esc}}$  held true in the past. While it is clear that the large majority of pairs within the  $1\sigma$  error ellipse do not produce a bound system for  $> 2$  Gyr, it is interesting that some orbits with a bound pair in excess of several Gyr do exist within this error-space. A larger abundance of such orbits can be found at relative PMs that are more in the West direction than our measurements imply. So the combination of galaxy masses shown in this plot, while unlikely, cannot be ruled out strictly based on the requirement that the LMC and SMC must have been bound for at least 2 Gyr. However, it should be noted that this does not imply that traditional models for the Magellanic Stream (which have often used masses such as shown in this figure) are tenable, because such models produce orbital periods that are inconsistent with the age of the Stream (discussed more below).

In summary, perhaps unsurprisingly, we find that to obtain long-lived binary LMC-SMC orbits the LMC mass must be relatively high, and the MW mass must be relatively low. The lower mass of the MW implies that the Clouds are on a first infall and, as such, the MW’s tidal field would be insufficient to disrupt the binary pair. We are more readily able to find such long-lived orbits with the new LMC center derived here rather than that previously derived by vdM02. We also find that a close encounter between the Clouds in the recent past is a generic result.

Given that the Clouds are a binary pair, the more massive LMC sets the orbital period for the Clouds about the MW. As shown above, the LMC mass must be  $\gtrsim 1 \times 10^{11} M_{\odot}$  for the Clouds to have been a long-term binary system. The smallest orbital periods about the

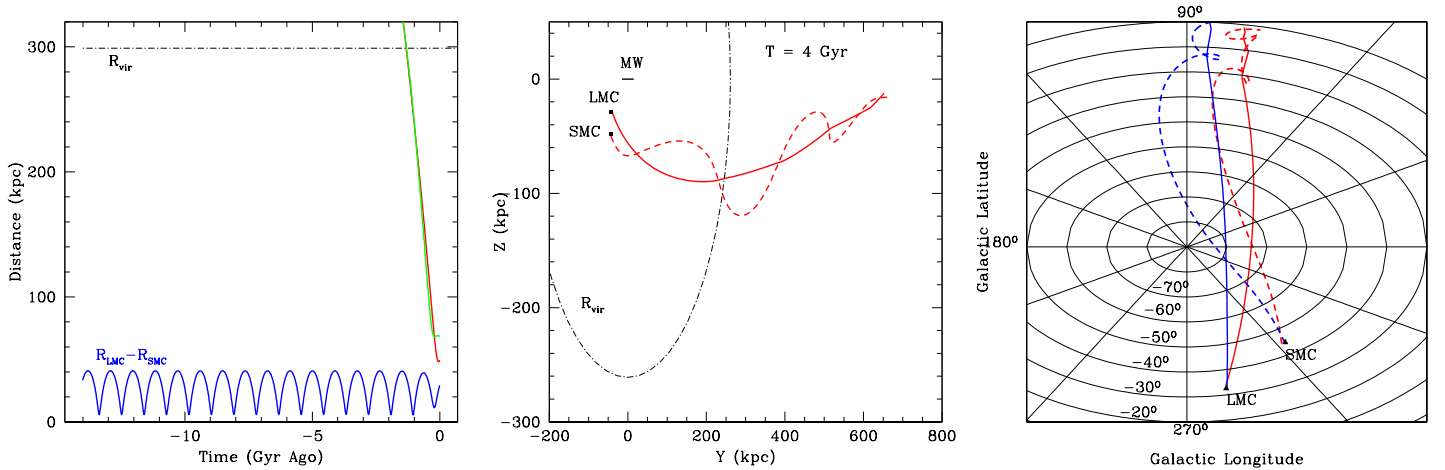


**Figure 13.** *Left:* Evolution of the LMC (red) and SMC (green) Galactocentric radius as a function of time in the past, for our canonical orbit, i.e.,  $M_{\text{vir}} = 1.5 \times 10^{12} M_{\odot}$ ,  $M_{\text{LMC}} = 1.8 \times 10^{11} M_{\odot}$ ,  $M_{\text{SMC}} = 3 \times 10^9 M_{\odot}$ , and the mean third epoch LMC velocity. The blue line shows the relative distance between the two Clouds. The dot-dash horizontal line shows the virial radius,  $R_{\text{vir}}$ , for this MW model. *Middle:* the same shown in the Galactocentric ( $Y, Z$ )-plane. The orbits of the LMC (solid red line) and SMC (dashed red line) are followed for the past 4 Gyr, and their present locations with respect to the MW are marked with black squares. The MW center is marked and its disk orientation is indicated by the short dash.  $R_{\text{vir}}$  is also shown. *Right:* the same orbits for the LMC (solid red line) and SMC (dashed red line) are shown in the  $(l, b)$ -plane. The blue lines show the corresponding GN96 orbits, which were chosen by those authors to match the location of the HI in the Magellanic Stream (see Figure 9 of B07), and stands in for the Stream location here.

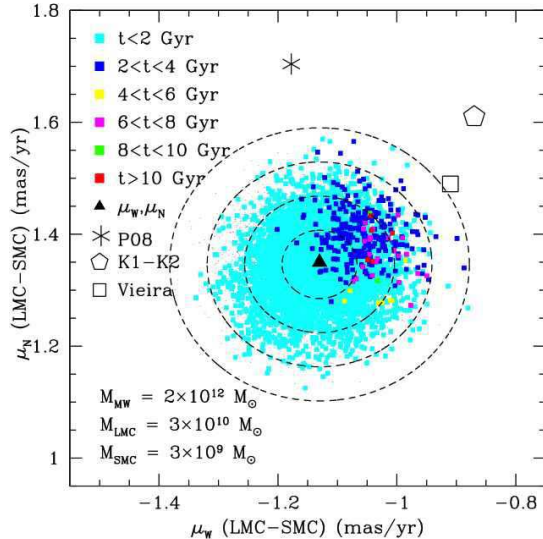


**Figure 14.** A further exploration of LMC-SMC orbits in a low-mass LMC and high-mass MW model (masses indicated in the figure). This combination of masses gives rise to more traditional LMC orbits (albeit with longer orbital periods as can be seen in Figure 11). We did 10,000 Monte Carlo drawings from the PM error distributions. We show the relative PM between the Clouds with each point color-coded by the amount of time for which  $V_{\text{LS}} < V_{\text{esc}}$  in the past (colored squares). The black triangle is the mean relative PM value from this study, with  $1\sigma$ ,  $2\sigma$ ,  $3\sigma$ , and  $4\sigma$  error ellipses indicated as well (dashed). While the vast majority of drawings do not give rise to orbits that were bound for more than 2 Gyr (cyan squares), there are some orbits that are bound for 2–4 Gyr within the  $1\sigma$  error ellipse (dark blue squares).

MW that we can obtain for such large LMC masses are in excess of 4 Gyr. This is problematic for models that rely on Milky Way tides to form the Stream, because age estimates of the Stream imply that the Stream is a young feature, much younger than 4 Gyr old. In fact, given the rate at which the Stream is being ablated away, as inferred from simulations of the observed anomalously high

$\text{H}\alpha$  emission in the Stream (Weiner & Williams 1996) by Bland-Hawthorn et al. (2007), and based on estimates of the survivability of high velocity clouds in MW-type environments (Heitsch & Putman 2009; Kereš & Hernquist 2009), it is unlikely that the Stream could have survived about the MW for more than  $\sim 1$ –2 Gyr.

The past orbit of the LMC and SMC, implied by the new velocities, is now better aligned with the location of the Stream HI than it was with the K1/K2 velocities. As discussed in B07, this is directly due to the lower value for  $\mu_N$ , which in turn is obtained here directly from the dynamical center of the LMC having changed with respect to what was used in K1. However, we note that the LMC orbit still does not trace the Stream closely: there remains a sizeable offset. The new SMC PMs, however, do allow the past SMC orbit to cross over the Stream location, which is now easier to reconcile with models where the Stream is largely stripped from the SMC (GN96; Růžička et al. 2010; Diaz & Bekki 2011; Besla et al. 2012) than it was with the K2 SMC PMs.

#### 6.4. First Infall?

As we learned from B07, the question of first infall is a model-dependent rather than simply a velocity-dependent one. We showed in that work that no matter whose velocities were used (K1/GN96/prior ground-based determinations), the Clouds were always on a first infall in a  $1.2 \times 10^{12} M_{\odot}$  NFW MW halo, and that in order to recapture something resembling the ‘traditional’ isothermal sphere orbit, we had to go to a  $2 \times 10^{12} M_{\odot}$  NFW halo.

Given that the new Galactocentric velocities derived here are lower than those in K1, we want to critically re-examine the arguments for whether the LMC may be on a first passage, which we define as an orbital solution wherein the LMC has first entered the virial radius of the MW within the past 1–4 Gyr and has not completed an orbit in that time. We have already shown

above that with our new velocities, a low LMC mass can make past pericentric passages about a high mass MW. Therefore, arguments for a first passage, being still model-dependent in nature, can be cast as arguments against a low-mass LMC and a high-mass MW. Our arguments fall into three main categories: (1) orbital eccentricity and cosmological expectations, (2) LMC tidal radius, and (3) LMC-SMC binarity. We also discuss a fourth argument that attempts to reconcile the high gas content and active star formation of the Clouds with their current close proximity to the MW.

**Orbital Eccentricity and Cosmological Expectations:** As shown in Figure 10 in all cases where the LMC does complete an orbit about the MW, the corresponding orbital periods are typically large ( $> 4$  Gyr). Such orbits take the LMC to apocentric distances of order the virial radius of the MW and thus imply large orbital eccentricities. The computed eccentricities for the  $3 \times 10^{10} M_{\odot}$  LMC and the  $2 \times 10^{10} M_{\odot}$  evolving MW model are 0.6–0.7. These eccentricities get higher for larger LMC masses. Comparing to Figure 5 of Boylan-Kolchin et al. (2011), only 20% of LMC analogs accreted at early times ( $> 8$  Gyr) have such orbits. Indeed, in the prevailing  $\Lambda$ CDM model of hierarchical structure formation, massive satellites that are accreted at early times are very rarely found on highly eccentric orbits about MW-type hosts at  $z=0$  (Boylan-Kolchin et al. 2011; Wetzel 2010; Stewart et al. 2008).

Generally, subhalos that are accreted on  $\sim$ radial orbits at early times are either preferentially destroyed or exist on more circularized orbits today (e.g., Benson 2005). While 50% of LMC analogs accreted more than 4 Gyr ago and 60% of LMC analogs accreted more than 8 Gyr ago have eccentricities  $< 0.5$  in the Millennium II sample, only 20% of LMC analogs accreted within the last 2–4 Gyr have such modest eccentricities (Boylan-Kolchin et al. 2011). A high MW mass, low LMC mass today isn’t ruled out from cosmological expectations, but the high eccentricities (0.6–0.7) calculated from our orbits are more typical of LMC analogs accreted within the past 4 Gyr. Therefore, from the eccentricities of our orbits, a first infall scenario for the Clouds is the favored orbital solution of  $\Lambda$ CDM theory.

We can also make a more general timing argument based on the fact that the Clouds and the MW must have been in close proximity at the time of the Big Bang (in analogy with similar arguments for e.g., M31 and Leo I (Li & White 2008)). This implies that the Clouds had a pericentric approach with the MW at the time of the Big Bang. So if there has been more than one complete orbit since, then the period must be  $< T_0/2$ , where  $T_0 = 13.73$  Gyr. Hence, orbits with a pericenter  $> 6.9$  Gyr ago are not physical, because the Clouds and MW were not together at the Big Bang. Of course, this is oversimplified for many reasons, e.g., the mass of the MW increases with time. But as we show in Figure 11, this typically increases the period by  $\sim 2$  Gyr. Therefore, finding an orbit that is consistent with the proper motion data with a pericenter at e.g., 10 Gyr ago, does not rule out a first infall scenario, since such orbits are not physical based on such a timing argument.

**LMC Tidal Radius:** As discussed in §6.1 the LMC total mass must be at least  $3 \times 10^{10} M_{\odot}$  from the Saha et al.

(2010) observations. Muñoz et al. (2006) have claimed a detection of LMC stars out to 20 kpc. If stars do indeed exist out to 20 kpc, the required LMC mass is  $\sim 8 \times 10^{10} M_{\odot}$ . It should be pointed out that more traditional Magellanic Stream models (GN96; Diaz & Bekki 2012) assume a total LMC mass of  $1 \times 10^{10} M_{\odot}$  which is already ruled out by the observations. Their choice of LMC mass is important to point out since this is the reason their orbital periods are so different from ours.

**LMC-SMC Binarity:** Studies of the star-formation histories of the Clouds all agree on the fact that the star-formation rate started to increase  $\sim 4$ –6 Gyr ago, and was quiescent in both galaxies before this time (Harris & Zaritsky 2009; Cignoni et al. 2012). The coincident increase in star-formation in both galaxies may imply that they were in a common envelope at the time, and corresponds to the epoch that the LMC captured the SMC in the Besla et al. (2012) model.

If we therefore take the stance that the two Clouds must have fallen into the MW as a bound system (although they need not necessarily be bound *at present*) we find that we are able to place limits on both the MW and LMC galaxy masses. We find that in general an LMC mass  $> 1 \times 10^{11} M_{\odot}$  is needed for the SMC to have been bound to the LMC for  $> 2$  Gyr in the past, and that further a MW mass  $< 1.5 \times 10^{12} M_{\odot}$  is required. Note that LMC orbits at this particular mass are almost always on first infall regardless of MW mass. The LMC mass required to keep the SMC bound to it goes up as the mass of the MW increases, in order to compensate for the increasing tidal field of the MW. But as the LMC mass increases the orbital eccentricity does as well, making a first infall scenario more likely based on the plausibility argument above that high eccentricities and early infall times are relatively rare in cosmological simulations.

It is harder to maintain a LMC-SMC binary for long periods of time in high mass MW and low mass LMC models: less than 5% of the 10,000 searched Monte Carlo cases result in binary configurations, meaning such models generally require that the LMC capture the SMC while in orbit about the MW - a statistically improbable event. This argument implies that the MW’s mass is likely less than  $2 \times 10^{12} M_{\odot}$ .

**The Clouds and the Morphology-Distance relation:** van den Bergh (2006) argued for a recent accretion of the Clouds, based on a comparison of the morphologies of MW and M31 satellites that showed that the Clouds are the only gas-rich dIrr galaxies at small Galactocentric distances, all other dIrrs being at large distances from their respective hosts. Some recent studies have looked at this issue from a larger statistical/cosmological point-of-view.

Tollerud et al. (2011) study a volume-limited spectroscopic sample of isolated galaxies in SDSS and find that bright satellite galaxies around MW-type hosts are significantly redder than typical galaxies in a similar luminosity range, and argue that this is indicative of environmental quenching. This is found to be in stark contrast to the LMC, which is anomalously blue in comparison to other LMC-MW analogs in SDSS. The authors attribute this to the fact that the LMC may be undergoing a triggered star formation event upon first infall.

Geha et al. (2012) have used the NASA-Sloan Atlas

to demonstrate that dwarf galaxies in the field (with masses in the LMC range) all have active star-formation ( $< 0.06\%$  of field-dwarfs in their sample have no star-formation). By contrast, the majority of quenched galaxies are all within 2–4 virial radii of a massive host. Therefore, ending star-formation in such dwarf galaxies appears to require the presence of a more massive neighbor. Had the Clouds been accreted early in the Universe then, it is unlikely that these galaxies would currently have as much gas or star formation as they do.

Wetzell et al. (2012) used SDSS galaxy group/cluster catalogs together with N-body simulations to look at the quenching timescales of satellites at  $z \sim 0$ . They find a quenching scenario in which satellite star-formation histories are unaffected for 2–4 Gyr after infall but then quench rapidly (with an e-folding time of  $< 0.8$  Gyr). Interestingly, because of the time delay before quenching starts, satellites are found to experience significant stellar mass growth after infall, which the authors point to as a key reason for the success of the subhalo abundance matching technique: supporting the larger LMC masses that we favor in this study.

In conclusion, despite the revised lower estimates for the 3D velocities of the Magellanic Clouds presented in this work, taken together, Figures 9, 10, 11, and 12 make a strong case for a first infall scenario. This conclusion draws largely from a recognition that the fundamental change to our understanding of the orbital history of the Clouds comes not only from the PMs, but also from a cosmologically motivated understanding of the mass evolution and dark matter halo profile of our MW. This picture is thus consistent with the theory that the origin of the large scale gaseous structures of the Magellanic System (Stream, Bridge and Leading Arm) and the internal structure and kinematics of the Clouds are a result of interactions between the LMC and SMC in a first infall scenario, rather than interactions with the MW (Besla et al. 2010, 2012).

## 7. CONCLUSIONS AND DISCUSSION

We have analyzed a new third epoch of data of 10 QSOs behind the LMC and 3 behind the SMC with WFC3/UVIS (one LMC field, L22, has only first epoch ACS and third epoch UVIS data). We combine these data with previously obtained ACS/HRC data giving a  $\sim 7$  yr baseline, in order to measure PMs for both Clouds, and to refine and validate measurements that used only two epochs over a 2 yr baseline (K1, K2, P08). We have also reanalyzed the first two epochs of data for 21 LMC fields and 5 SMC fields, using a method to account for the degrading CTE of the HRC as well as an improved approach to linear transformations. Here we summarize our findings, the implications for the Clouds’ orbits, and provide a look ahead to the future.

### 7.1. Conclusions for COM PMs and Galactocentric Velocities

The ACS reanalysis and the third epoch analysis give very consistent results at the level of the measured per-field PMs. In order to obtain COM PMs from these field PMs, the geometry and internal motions of the L/SMC need to be taken into account. The addition of the WFC3 epoch provides very small per-field PM errors of  $\sim 0.03$  mas yr $^{-1}$  (7 km s $^{-1}$ , or 1.6% of the total

PM). We are therefore able to independently constrain all parameters of the LMC PM rotation field, including the inclination,  $i$ , the position angle of the line-of-nodes,  $\theta$ , the dynamical center, rotation velocity amplitude, and even the distance. This is a big improvement over K1. This procedure and the results are discussed in detail in Paper II. The features of import for the present study are that we obtain a rotation velocity that agrees very well with that obtained independently by Olsen et al. (2011) using a very large number of LOS velocities of stellar tracers. Moreover, we find strong evidence that the center of the LMC (as obtained from the PM fit to the rotation field) is consistent with the HI dynamical center, and not the center derived by vdM02, which agrees with the brightest part of the LMC bar.

For the SMC, the sparse coverage of QSO fields renders it difficult to gain much insight into its geometry. We therefore fit a relatively simple model to the SMC PM data, which allows for viewing perspective and a single overall rotation of the SMC in the plane of the sky. The old stellar population in the SMC shows little evidence for rotation (Harris & Zaritsky 2006) so we base our analysis of the SMC COM PM on the assumption that  $V_{\text{rot}} = 0 \pm 15$  km s $^{-1}$ . Analyses in which  $V_{\text{rot}}$  is instead fit to the PM data do not yield a significantly different answer.

If we analyze the new LMC PM data with the same fixed geometric parameters as used in vdM02 we obtain a COM PM whose (i) value for  $\mu_W$  is lower, but consistent within  $1.6\sigma$  with the K1 result, (ii) value for  $\mu_N$  remains unchanged with respect to K1, (iii) random errors are smaller by a factor of almost 5 than K1. If we analyze the PM data with the LMC model derived from the data itself, which is the preferred approach, then the value of  $\mu_W$  and its random error remain largely unchanged. However, the value for  $\mu_N$  changes significantly (by  $4\sigma$ ), and its random error increases by a factor of almost 3. For the SMC, the three-epoch analysis agrees with K2 for  $\mu_N$ , while for  $\mu_W$  it differs by  $2.4\sigma$ . This is largely due to how fields were combined in K2 and not due to intra-field differences. Our final SMC COM PM value is in rough agreement with the results of P08.

We attempt here to give as accurate an estimate as possible of the observational random errors in the COM PM, by propagating all unknowns in the geometry as well as the PM determination. This obviously increases errors with respect to previous studies which only propagated PM errors. Remarkably, the PM data are now no longer the dominant source of uncertainty, but rather uncertainties in the structure of the Clouds, dominate how well the COM PM can be established. Our final COM measurement errors, listed in line 1 of Table 4, do not represent a huge improvement over what was listed in previous HST works, despite the significantly improved accuracy of the present work. However, this is because those previous works underestimated the true random errors. Regardless, the uncertainty in the inferred transverse velocities of the Clouds are now dominated by their distance uncertainties, and not their COM PM uncertainties.

In order to turn the measured COM PMs into Galactocentric velocities, we need to know the solar velocity. Our understanding of the solar velocity has recently been revised upwards, and this works to directly reduce the Galactocentric velocities of the Clouds by

a comparable amount. Therefore, the Galactocentric  $v_{\text{tot}} = 321 \pm 24 \text{ km s}^{-1}$  for the LMC presented here is  $57 \text{ km s}^{-1}$  lower than that in K1, owing roughly equally to the decrease in  $\mu_W$  described above and to the increase in solar velocity. There is a much smaller dependence on the new dynamical center derived here (see Table 5). The new center affects mainly the  $\mu_N$  value, which determines the location of the orbit in projection on the sky rather than the tangential velocity (as described in B07). By contrast, if we use the same geometric model and solar velocity (IAU value) used in K1,  $v_{\text{tot}}$  decreases by  $31 \text{ km s}^{-1}$  compared to the K1 value, which is comparable to the size of the  $1\sigma$  error bar.

The SMC's inferred  $v_{\text{tot}} = 217 \pm 26 \text{ km s}^{-1}$  is  $85 \text{ km s}^{-1}$  lower than in K2. This is due mainly to the new proper motion derived here (which itself is due to how the fields were combined in K2, rather than differences in the derived per-field PMs). Roughly  $20 \text{ km s}^{-1}$  of the decrease in  $v_{\text{tot}}$  is due to the revised solar velocity, and there is also a small contribution from the different SMC center used here, compared to the K2 analysis.

### 7.2. Conclusions for the Clouds' Implied Orbits

Given the new velocities obtained here, we have re-evaluated the past orbital histories of the Clouds about the MW. We find that the dominant unknowns are the MW and LMC masses. However, some reasonable arguments allow us to narrow down the allowed ranges of MW and LMC masses. The results continue to make a strong case, as first argued in B07, that the Clouds are likely on their first infall into the MW.

From the search for bound orbits between the two Clouds (see Figure 12), we are able to identify a combination of masses that satisfy the criterion of long-lived binarity, and also produces orbits around the MW that are plausible from a cosmological point of view (Boylan-Kolchin et al. 2011; Busha et al. 2011a). This yields a preferred MW mass,  $\lesssim 1.5 \times 10^{12} M_{\odot}$ . The probability of a stable LMC-SMC binary configuration decreases as the MW mass increases. An LMC mass  $\gtrsim 1 \times 10^{11} M_{\odot}$  is needed in order to keep the SMC bound to the LMC for a reasonable fraction of a Hubble time. Taken together, this combination of MW and LMC masses imply that the LMC/the Clouds are on their first infall (see Figure 9).

From a cosmological point of view, these orbits do not represent a major alteration to the interpretation given in B07. Here we have explored a more full set of mass models for the LMC. The inferred LMC mass agrees with the expected total infall mass of the LMC, as calculated from the observed present-day stellar mass (vdM02) and the relations from halo occupation models (Guo et al. 2010; Sales et al. 2011). A generic outcome of our study is that regardless of what MW mass is used, large LMC masses are always on a first infall.

We have also implemented a simple model for the expected mass evolution of the MW over the past  $\sim 10$  Gyr. This, as might be expected, significantly increases the periods of LMC orbits that do make a previous pericentric passage (higher MW mass models), i.e., the orbits are highly eccentric. In a recent study, motivated by the discussion over the higher Solar velocity, Zhang et al. (2012) have also revisited the Clouds' past orbital history, uti-

lizing numerical simulations to explore the evolution of the MW. Like us here, they find that it is possible for the LMC to make past pericentric passages given the observational and theoretical error-space. They do not vary LMC mass (it is kept fixed at  $2 \times 10^{10} M_{\odot}$ ), or investigate whether binarity imposes constraints, so we cannot directly compare our results with theirs, but were we to use such a low LMC mass, our studies would likely be consistent.

We put forth four arguments why we think orbits in which the LMC/SMC make a previous pericentric passage are implausible. One is the expected eccentricities of orbits from cosmological simulations along with a simple version of the timing argument (see § 6.4), the second is the tidal radius of the LMC, and the third is the fact that long-lived SMC-LMC binary configurations have lower probability for such orbits, given the observed COM PMs of the Clouds. The fourth argument derives from the work of van den Bergh (2006) who conducted a morphological comparison of the satellites of the MW and M31, finding that the L/SMC are the only two gas-rich dIrrs at close Galactocentric distance to a host. He argues that they may be interlopers from a remote part of the Local Group rather than true satellites of the MW.

This line of argument is also consistent with the fact that LMC-SMC-MW analogs are relatively rare today in our local volume (Liu et al. 2011) and in cosmological simulations at  $z=0$  (Boylan-Kolchin et al. 2011). MW-type hosts are efficient at tidally disrupting such bound configurations. Furthermore, Tollerud et al. (2011) find that, compared to other R-band selected LMC-MW analogs in SDSS, the LMC is unusually blue in color. This fact is reconcilable in a first infall scenario where the LMC is accreted recently, because it has been able to retain enough gas to maintain a high star formation rate today (see also Wetzel et al. 2012). However, Tollerud et al. (2011) also find that the LMC's color is unusual compared to R-band selected LMC analogs in the field. Besla et al. (2012) present a theory in which the star formation rate of both the LMC and SMC has increased recently owing to interactions between these two galaxies. Given that LMC-SMC configurations are rare in general, it is thus unsurprising that the overall star formation rate of the LMC is higher than average isolated analogs.

Even in the case for the most long-lived LMC-MW configuration presented here (i.e., low LMC mass and high MW mass) the LMC makes at best  $\sim 2$  past pericentric passages (see Figure 9). The long implied orbital periods exceed the lifetime of the Magellanic Stream (1–2 Gyr) (e.g., Heitsch & Putman 2009; Kereš & Hernquist 2009). This conclusion is consistent with our arguments for the need for a new formation mechanism for the Magellanic Stream that does not rely on a previous pericentric approach about the MW. Moreover, such a combination of LMC and MW masses make it difficult for the LMC and SMC to have been a long-lived binary system.

The existence of the LMC-SMC system as a binary for more than 2 Gyr in the past favors a combination of a high mass LMC and an intermediate or low mass MW. Our work has found that such configurations always yield first infall orbital configurations. We show an example of an orbit that fulfills all the criteria set out above in Figure 13. This shows that viable orbital solutions can

be found that are consistent with both the *HST* PMs and cosmological expectations. The new SMC PM now allows the past orbit of the SMC to cross-over the location of the HI in the Stream, which was very difficult to obtain with the old K2 PMs and is consistent with a picture in which the Stream is formed primarily by the removal of material from the SMC (GN96; Connors et al. 2006; Besla et al. 2010, 2012; Diaz & Bekki 2011, 2012).

### 7.3. Future Work

Recently the sample of QSOs behind the Magellanic Clouds has increased drastically. There are now well over 200 newly identified QSOs behind the LMC and 29 behind the SMC. The new QSOs were selected primarily based on their mid-IR colors (Kozłowski & Kochanek 2009). The majority of them were spectroscopically confirmed from follow-up data taken with 2DF/AAOMEGA (Kozłowski et al. 2011, 2012), while a smaller subset (around 40) were confirmed with Magellan/IMACS (by N. Kallivayalil & M. Geha). PM studies of fields around a carefully chosen subset of these QSOs could vastly improve our knowledge of the structure and dynamics of the Clouds.

With a larger sample of QSOs homogeneously distributed behind the SMC, we can investigate its rotation and structure, something we have been unable to tackle with only 5 QSO fields thus far (and with only 3 QSOs currently imaged with WFC3/UVIS). A larger number of QSOs will also improve our knowledge of its COM PM.

For the LMC, a large number of fields with PMs would allow us to better sample the rotation curve, including its inner slope. The increased coverage would also allow us to combine our PMs with radial velocity studies (e.g., Parisi et al. 2010; Olsen et al. 2011), thereby constituting a unique 3D data-set. With a large number of QSO fields we may also be able to distinguish between the kinematics of different stellar populations within the LMC directly.

Finally, with exposures of sufficient depth, it is possible to measure absolute PMs with resolved background galaxies (Sohn et al. 2012), so we should not be confined to fields with QSOs. We are in the process of identifying fields in the Clouds with deep *HST*/*ACS* exposures in an earlier epoch, which should have numerous background galaxies that can be used to yield an accurate absolute PM of the stars in the field.

## APPENDIX

### WFPC2/PC DATA

A third epoch of *HST* imaging of our QSO fields was originally due to execute on *ACS*/*HRC* in the period July 2007 to November 2008. However, due to the failure of *ACS* at that time, the observations were executed on the Planetary Camera (PC) of the *WFPC2* instrument (PID 11201). All of the 40 targets (34 LMC & 6 SMC QSO fields) that had been observed with *ACS*/*HRC* in epoch 1 were observed with *WFPC2* in snapshot mode, providing a typical time baseline of 5 years. The observational approach was similar to that in epochs 1 & 2. We used the *V*-band (F606W) filter and a 5 or 6-point dither pattern. Total exposure times ranged from 2.8 to 20 minutes.

The data were analyzed with similar techniques as used for the first two *ACS* epochs. A discussion of the analysis and results for a subset of the fields was presented in Kallivayalil et al. (2009b). In Figure 15 we show the position of the quasar over time, in a reference frame based on the 1st epoch images, for 4 randomly chosen LMC fields. The scatter among positions within the same epoch shows that the RMS error in the position of the quasar is roughly 3 times as large for *WFPC2* as for *ACS* ( $\sim 0.021$  HRC pixels versus 0.008 HRC pixels, respectively). The lower accuracy for *WFPC2* is due to a combination of several factors. These include the larger pixel size, lower sensitivity, and less well calibrated and stable geometric distortions for *WFPC2* compared to *ACS*/*HRC*.

The 40 fields for which *WFPC2* data were obtained fall in three categories:

- (1) 14 Fields for which two epochs of *ACS* data exist, but no *WFC3* data. For these fields the *WFPC2* data provide a useful consistency check, as evident from Figure 15. The *WFPC2* data more than double the time baseline and fall on the extrapolation of the *ACS* measured PMs. The use of a different instrument and the addition of a third epoch rule out a variety of potential systematic errors. However, as discussed in Kallivayalil et al. (2009b), the *WFPC2* data help very little to reduce the random PM errors in each field.
- (2) 13 Fields for which *ACS* data exist, as well as one epoch of *WFC3* data. For these fields the *WFC3* data provide superior accuracy and a longer time baseline. Hence, the *WFPC2* data do not provide anything in terms of additional insights or reduced PM errors.
- (3) 13 Fields for which only a first epoch of *ACS* data exists. For 11 of these fields the data provide the opportunity to determine a PM where none yet exists (2 fields are unsuitable as discussed in Appendix B). This might in principle help to obtain better spatial coverage of measurements within the LMC and SMC. However, we have found that the PM accuracy that can be achieved for these fields is relatively low. The random PM errors for 5-year *ACS*-*WFPC2* measurements are a factor 2–4 higher than for 2-year *ACS*-*ACS* measurements.

These considerations indicate that the *WFPC2* data are of insufficient quality to help better constrain the analysis presented in this paper. For this reason, we have not attempted to analyze the *WFPC2* data to the same level of detail and completion as for the other instruments, and we do not report and use the *WFPC2* results in this paper.

### OBSERVED FIELDS UNSUITABLE FOR PM DETERMINATION

We found that two QSO fields observed with *WFC3* proved unsuitable for PM determination of the Magellanic Clouds. These fields were not part of the K1 or K2 sample, but only had one epoch of previous *ACS* data (which had never been fully analyzed). We briefly discuss here the reasons for excluding these fields from the sample for the present paper.

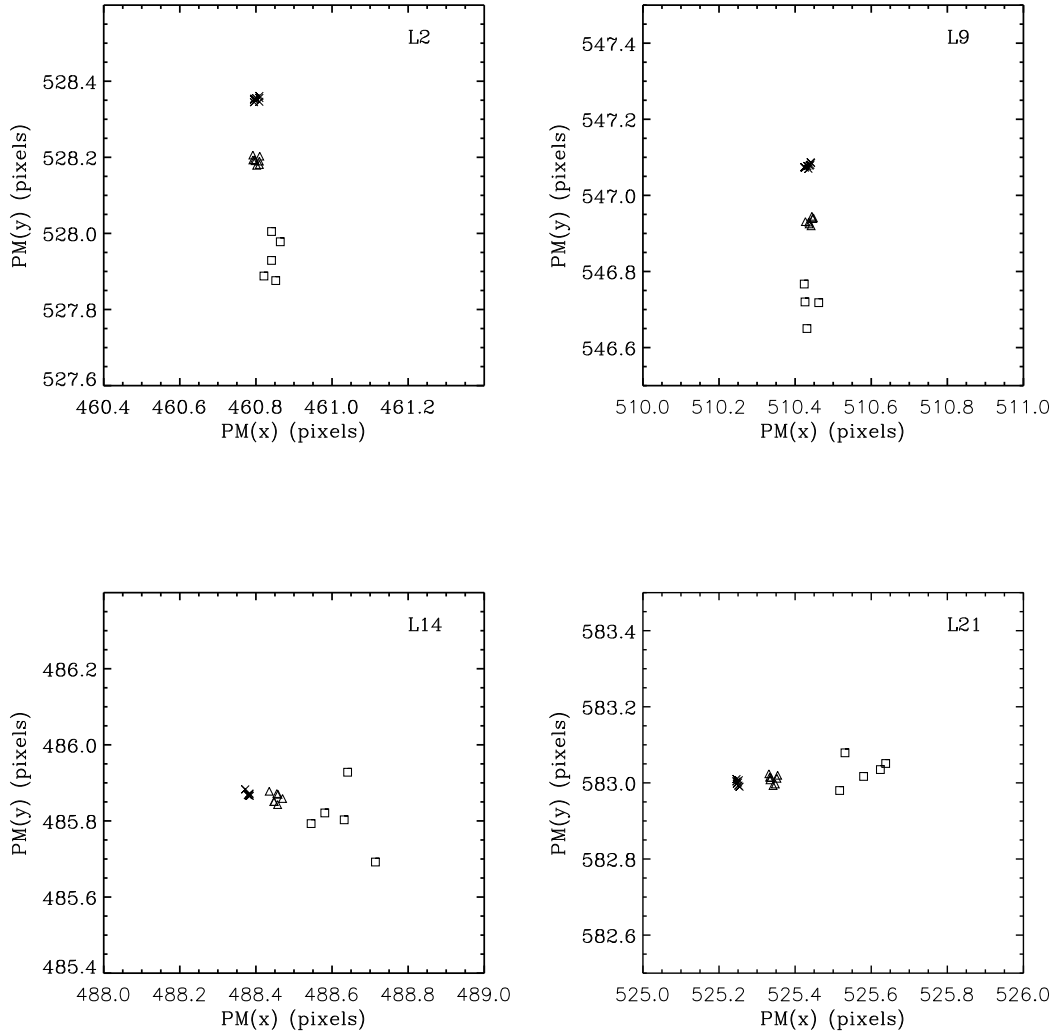


**Figure 15.** Positions, in a reference frame based on the 1st epoch images, of the quasar over time for 4 randomly chosen LMC fields showing ACS epoch 1 (*crosses*), ACS epoch 2 (*triangles*) and WFPC2/PC (*open squares*). The scatter per epoch gives the relative size of the RMS errors in the position of the quasar relative to the star-field, given that the observation has been repeated many times per epoch. Each panel is  $1 \times 1$  pixel (1 pix = 28 mas). North is in a different direction in each panel.

**RX J0524.0-7011:** This ROSAT X-Ray source at  $(\alpha, \delta) = (05h24m02.3s, -70d11m09s)$  was optically identified as an AGN at  $z = 0.15$  in the LMC background by Cowley et al. (1984). It was cross-identified as MACHO ID 006.07059.0207 by Geha et al. (2003). It has the lowest redshift in our sample, and is also relatively bright, with  $V = 17.7$ . In our WFC3 images the AGN is clearly resolved, and a spiral host galaxy is visible surrounding a point-like nucleus. The astrometric techniques used in this paper are not designed for extended sources, and application of these techniques was found not to produce reliable PM results for this target. We therefore excluded it from the sample.

**RX J0111.7-7250:** This ROSAT X-Ray source was included by Tinney et al. (1997) in a study aimed at finding QSOs behind the SMC. They aligned an optical spectrograph slit along the two bluest objects within a  $\sim 20''$  circle (believed to be a good guess for the ROSAT positional error) around the source. Neither of the objects turned out to be a background AGN. However, they detected a serendipitous background emission-line object along the slit at redshift  $z = 0.197$ . The object was called QJ0111-7249, and identified as an optical QSO. This seems tentative at best, given that the spectrum showed only Balmer emission lines (which leaves open the possibility for alternative categorizations). The emission-line object was  $23''$  from the ROSAT position at the time, only marginally consistent within the uncertainties. Subsequently, the X-ray source was included as #348 in the ROSAT PSPC catalogue of X-ray sources in the SMC region compiled by Haberl et al. (2000). They provided an improved position of  $(\alpha, \delta) = (01h11m40.9s - 72d50m28s)$  (J2000.0), with a 90% confidence random uncertainty of  $4.1''$  and an additional systematic uncertainty of  $\sim 7''$ . This position is  $41''$  from QJ0111-7249, and the sources therefore are not associated. Nonetheless, most literature has continued to treat the sources as one and the same. Our *HST* observations were centered on QJ0111-7249. Hence, the actual X-ray source did not fall in the ACS/HRC field of view. Our PM analysis of the

field did not reveal any point-like source with a reflex motion typical of a background reference source. Therefore, we conclude that QJ0111-7249 is not suitable for SMC PM determination, and exclude it from the sample. Interestingly, this same source was used by Costa et al. (2011) in their ground-based study of the SMC PM. They obtained a very discrepant motion for this SMC field,  $(\mu_W, \mu_N) = (-0.06, -0.71)$  mas yr<sup>-1</sup>, compared to their average based on the other fields,  $(-0.93, -1.25)$  mas yr<sup>-1</sup>. This supports our interpretation, although Costa et al. (2011) argue it may be due to streaming motions in the SMC.

Both of the targets discussed in this appendix are atypical in our sample, given that they were selected as previously known X-ray sources. The large majority of our sample studied in this paper is composed of QSOs from Geha et al. (2003), which were identified from their variability characteristics in the MACHO database, with subsequent spectroscopic follow-up.

We would like to thank Lars Hernquist, Mike Boylan-Kolchin, Marla Geha, Ana Bonaca, Luis Vargas, Nhung Ho, and Jeremy Bradford for useful discussions about this project as a whole. William van Altena, Dana Dinescu and Terry Girard provided valuable insight on per-field errors versus final errors for the center-of-mass motion. Support for this work was provided by NASA through grants associated with projects GO-11730 and GO-11201 from the Space Telescope Science Institute (STScI), which is operated by the Association of Universities for Research in Astronomy, Inc., under NASA contract NAS 5-26555. GB acknowledges support from NASA through Hubble Fellowship grant HST-HF-51284.01-A.

## REFERENCES

- Anderson, J. & Bedin, L. R. 2010, *PASP*, 122, 1035  
 Anderson, J. & King, I. R. 2004, Multi-filter PSFs and Distortion Corrections for the HRC, Instrument Science Report ACS 2004-15  
 Bekki, K. 2008, *ApJ*, 684, L87  
 Bekki, K. 2011, *ApJ*, 730, L2  
 Bekki, K. & Chiba, M. 2005, *MNRAS*, 356, 680  
 Bellini, A., Anderson, J., & Bedin, L. R. 2011, *PASP*, 123, 622  
 Benson, A. J. 2005, *MNRAS*, 358, 551  
 Besla, G., Kallivayalil, N., Hernquist, L., Robertson, B., Cox, T. J., van der Marel, R. P., & Alcock, C. 2007, *ApJ*, 668, 949  
 Besla, G., Kallivayalil, N., Hernquist, L., van der Marel, R. P., Cox, T. J., & Kereš, D. 2010, *ApJ*, 721, L97  
 Besla, G., Kallivayalil, N., Hernquist, L., van der Marel, R. P., Cox, T. J., & Kereš, D. 2012, *MNRAS*, 421, 2109  
 Bland-Hawthorn, J., Sutherland, R., Agertz, O., & Moore, B. 2007, *ApJ*, 670, L109  
 Bovy, J., Allende Prieto, C., Beers, T. C., et al. 2012, *ApJ*, 759, 131  
 Boylan-Kolchin, M., Besla, G., & Hernquist, L. 2011, *MNRAS*, 414, 1560  
 Boylan-Kolchin, M., Springel, V., White, S. D. M., & Jenkins, A. 2010, *MNRAS*, 406, 896  
 Brüns, C., Kerp, J., Staveley-Smith, L., Mebold, U., Putman, M. E., Haynes, R. F., Kalberla, P. M. W., Muller, E., & Filipovic, M. D. 2005, *A&A*, 432, 45  
 Busha, M. T., Marshall, P. J., Wechsler, R. H., Klypin, A., & Primack, J. 2011a, *ApJ*, 743, 40  
 Busha, M. T., Wechsler, R. H., Behroozi, P. S., Gerke, B. F., Klypin, A. A., & Primack, J. R. 2011b, *ApJ*, 743, 117  
 Cignoni, M., Cole, A. A., Tosi, M., Gallagher, J. S., Sabbi, E., Anderson, J., Grebel, E. K., & Nota, A. 2012, *ArXiv e-prints*  
 Cioni, M.-R. L., van der Marel, R. P., Loup, C., & Habing, H. J. 2000, *A&A*, 359, 601  
 Connors, T. W., Kawata, D., & Gibson, B. K. 2006, *MNRAS*, 371, 108  
 Costa, E., Méndez, R. A., Pedreros, M. H., Moyano, M., Gallart, C., & Noël, N. 2011, *AJ*, 141, 136  
 Costa, E., Méndez, R. A., Pedreros, M. H., Moyano, M., Gallart, C., Noël, N., Baume, G., & Carraro, G. 2009, *AJ*, 137, 4339  
 Cowley, A. P., Crampton, D., Hutchings, J. B., Helfand, D. J., Hamilton, T. T., Thorstensen, J. R., & Charles, P. A. 1984, *ApJ*, 286, 196  
 Crowl, H. H., Sarajedini, A., Piatti, A. E., Geisler, D., Bica, E., Clariá, J. J., & Santos, Jr., J. F. C. 2001, *AJ*, 122, 220  
 Dehnen, W. & Binney, J. 1998, *MNRAS*, 294, 429  
 Diaz, J. & Bekki, K. 2011, *MNRAS*, 413, 2015  
 Diaz, J. D. & Bekki, K. 2012, *ApJ*, 750, 36  
 Evans, C. J. & Howarth, I. D. 2008, *MNRAS*, 386, 826  
 Fakhouri, O., Ma, C.-P., & Boylan-Kolchin, M. 2010, *MNRAS*, 406, 2267  
 Freedman, W. L., Madore, B. F., Gibson, B. K., Ferrarese, L., Kelson, D. D., Sakai, S., Mould, J. R., Kennicutt, Jr., R. C., Ford, H. C., Graham, J. A., Huchra, J. P., Hughes, S. M. G., Illingworth, G. D., Macri, L. M., & Stetson, P. B. 2001, *ApJ*, 553, 47  
 Gardiner, L. T. & Noguchi, M. 1996, *MNRAS*, 278, 191  
 Geha, M., Alcock, C., Allsman, R. A., Alves, D. R., Axelrod, T. S., Becker, A. C., Bennett, D. P., Cook, K. H., Drake, A. J., Freeman, K. C., Griest, K., Keller, S. C., Lehner, M. J., Marshall, S. L., Minniti, D., Nelson, C. A., Peterson, B. A., Popowski, P., Pratt, M. R., Quinn, P. J., Stubbs, C. W., Sutherland, W., Tomaney, A. B., Vandehi, T., & Welch, D. L. 2003, *AJ*, 125, 1  
 Geha, M., Blanton, M., Yan, R., & Tinker, J. 2012, *ApJ*, 757, 85  
 Gnedin, O. Y., Brown, W. R., Geller, M. J., & Kenyon, S. J. 2010, *ApJ*, 720, L108  
 Gnedin, O. Y., Kravtsov, A. V., Klypin, A. A., & Nagai, D. 2004, *ApJ*, 616, 16  
 Guo, Q., White, S., Li, C., & Boylan-Kolchin, M. 2010, *MNRAS*, 404, 1111  
 Haberl, F., Filipović, M. D., Pietsch, W., & Kahabka, P. 2000, *A&AS*, 142, 41  
 Harris, J. & Zaritsky, D. 2006, *AJ*, 131, 2514  
 Harris, J. & Zaritsky, D. 2009, *AJ*, 138, 1243  
 Heitsch, F. & Putman, M. E. 2009, *ApJ*, 698, 1485  
 Hernquist, L. 1990, *ApJ*, 356, 359  
 Kallivayalil, N., Besla, G., Sanderson, R., & Alcock, C. 2009a, *ApJ*, 700, 924  
 Kallivayalil, N., van der Marel, R. P., & Alcock, C. 2006a, *ApJ*, 652, 1213  
 Kallivayalil, N., van der Marel, R. P., Alcock, C., Axelrod, T., Cook, K. H., Drake, A. J., & Geha, M. 2006b, *ApJ*, 638, 772  
 Kallivayalil, N., van der Marel, R. P., Anderson, J., Besla, G., & Alcock, C. 2009b, in *IAU Symposium*, Vol. 256, IAU Symposium, ed. J. T. van Loon & J. M. Oliveira, 93–98  
 Kereš, D. & Hernquist, L. 2009, *ApJ*, 700, L1

- Kerr, F. J. & Lynden-Bell, D. 1986, *MNRAS*, 221, 1023
- Kim, S., Staveley-Smith, L., Dopita, M. A., Freeman, K. C., Sault, R. J., Kesteven, M. J., & McConnell, D. 1998, *ApJ*, 503, 674
- Klypin, A. A., Trujillo-Gomez, S., & Primack, J. 2011, *ApJ*, 740, 102
- Kozłowski, S. & Kochanek, C. S. 2009, *ApJ*, 701, 508
- Kozłowski, S., Kochanek, C. S., Jacyszyn, A. M., Udalski, A., Szymański, M. K., Poleski, R., Kubiak, M., Soszyński, I., Pietrzyński, G., Wyrzykowski, L., Ulaczyk, K., & Pietrukowicz, P. 2012, *ApJ*, 746, 27
- Kozłowski, S., Kochanek, C. S., & Udalski, A. 2011, *ApJS*, 194, 22
- Li, Y.-S. & White, S. D. M. 2008, *MNRAS*, 384, 1459
- Liu, L., Gerke, B. F., Wechsler, R. H., Behroozi, P. S., & Busha, M. T. 2011, *ApJ*, 733, 62
- Maller, A. H. & Bullock, J. S. 2004, *MNRAS*, 355, 694
- Mastropietro, C., Moore, B., Mayer, L., Wadsley, J., & Stadel, J. 2005, *MNRAS*, 363, 509
- Mathewson, D. S., Cleary, M. N., & Murray, J. D. 1974, *ApJ*, 190, 291
- McMillan, P. J. 2011, *MNRAS*, 414, 2446
- Miyamoto, M. & Nagai, R. 1975, *PASJ*, 27, 533
- Moore, B. & Davis, M. 1994, *MNRAS*, 270, 209
- Moster, B. P., Naab, T., & White, S. D. M. 2012, *MNRAS*, 321
- Muñoz, R. R., Majewski, S. R., Zaggia, S., Kunkel, W. E., Frinchaboy, P. M., Nidever, D. L., Crnojevic, D., Patterson, R. J., Crane, J. D., Johnston, K. V., Sohn, S. T., Bernstein, R., & Shectman, S. 2006, *ApJ*, 649, 201
- Murai, T. & Fujimoto, M. 1980, *PASJ*, 32, 581
- Nidever, D. L., Majewski, S. R., Butler Burton, W., & Nigra, L. 2010, *ApJ*, 723, 1618
- Olsen, K. A. G. & Massey, P. 2007, *ApJ*, 656, L61
- Olsen, K. A. G., Zaritsky, D., Blum, R. D., Boyer, M. L., & Gordon, K. D. 2011, *ApJ*, 737, 29
- Parisi, M. C., Geisler, D., Grocholski, A. J., Clariá, J. J., & Sarajedini, A. 2010, *AJ*, 139, 1168
- Piatek, S., Pryor, C., & Olszewski, E. W. 2008, *AJ*, 135, 1024
- Putman, M. E., Staveley-Smith, L., Freeman, K. C., Gibson, B. K., & Barnes, D. G. 2003, *ApJ*, 586, 170
- Reid, M. J. & Brunthaler, A. 2004, *ApJ*, 616, 872
- Reid, M. J., Menten, K. M., Zheng, X. W., Brunthaler, A., Moscadelli, L., Xu, Y., Zhang, B., Sato, M., Honma, M., Hirota, T., Hachisuka, K., Choi, Y. K., Moellenbrock, G. A., & Bartkiewicz, A. 2009, *ApJ*, 700, 137
- Rocha, M., Peter, A. H. G., & Bullock, J. S. 2012, *MNRAS*, 425, 231
- Růžička, A., Theis, C., & Palouš, J. 2009, *ApJ*, 691, 1807
- Růžička, A., Theis, C., & Palouš, J. 2010, *ApJ*, 725, 369
- Saha, A., Olszewski, E. W., Brondel, B., Olsen, K., Knezek, P., Harris, J., Smith, C., Subramaniam, A., Claver, J., Rest, A., Seitzer, P., Cook, K. H., Minniti, D., & Suntzeff, N. B. 2010, *AJ*, 140, 1719
- Sales, L. V., Navarro, J. F., Cooper, A. P., White, S. D. M., Frenk, C. S., & Helmi, A. 2011, *MNRAS*, 418, 648
- Schönrich, R., Binney, J., & Dehnen, W. 2010, *MNRAS*, 403, 1829
- Shattow, G. & Loeb, A. 2009, *MNRAS*, 392, L21
- Sohn, S. T., Anderson, J., & van der Marel, R. P. 2012, *ApJ*, 753, 7
- Stanimirović, S., Staveley-Smith, L., & Jones, P. A. 2004, *ApJ*, 604, 176
- Stewart, K. R., Bullock, J. S., Wechsler, R. H., Maller, A. H., & Zentner, A. R. 2008, *ApJ*, 683, 597
- Tinney, C. G., Da Costa, G. S., & Zinnecker, H. 1997, *MNRAS*, 285, 111
- Tollerud, E. J., Boylan-Kolchin, M., Barton, E. J., Bullock, J. S., & Trinh, C. Q. 2011, *ApJ*, 738, 102
- van den Bergh, S. 2006, *AJ*, 132, 1571
- van der Marel, R. P. 2006, in *The Local Group as an Astrophysical Laboratory*, ed. M. Livio & T. M. Brown, 47–71
- van der Marel, R. P., Alves, D. R., Hardy, E., & Suntzeff, N. B. 2002, *AJ*, 124, 2639
- van der Marel, R. P. & Cioni, M.-R. L. 2001, *AJ*, 122, 1807
- van der Marel, R. P., Kallivayalil, N., & Besla, G. 2009, in *IAU Symposium*, Vol. 256, *IAU Symposium*, ed. J. T. van Loon & J. M. Oliveira, 81–92
- Vieira, K., Girard, T. M., van Altena, W. F., Zacharias, N., Casetti-Dinescu, D. I., Korchagin, V. I., Platais, I., Monet, D. G., López, C. E., Herrera, D., & Castillo, D. J. 2010, *AJ*, 140, 1934
- Wannier, P. & Wrixon, G. T. 1972, *ApJ*, 173, L119
- Weiner, B. J. & Williams, T. B. 1996, *AJ*, 111, 1156
- Wetzel, A. R. 2010, PhD thesis, University of California, Berkeley
- Wetzel, A. R., Tinker, J. L., Conroy, C., & van den Bosch, F. C. 2012, arXiv:1206.3571
- Yang, Y. & Hammer, F. 2010, *ApJ*, 725, L24
- Yoshizawa, A. M. & Noguchi, M. 2003, *MNRAS*, 339, 1135
- Zhang, X., Lin, D. N. C., Burkert, A., & Oser, L. 2012, *ApJ*, 759, 99

**Table 1**  
LMC Observations and PM Results

ID	RA	DEC	$T$	$\Delta time$	$N$	PM of FIELD AS OBSERVED								LMC PM(CM) estimate	
						$\mu_W$	$\mu_N$	$\delta\mu_W$	$\delta\mu_N$	$\mu_W$	$\mu_N$	$\delta\mu_W$	$\delta\mu_N$	$\mu_W$	$\mu_N$
	(H,M,S)	(deg, ', ")	(min)	(yr)		2-epoch PMs ( mas yr <sup>-1</sup> )				3-epoch PMs ( mas yr <sup>-1</sup> )				( mas yr <sup>-1</sup> )	
L1	5 47 50.2	-67 28 1.3	2.6	7.1	8	-1.491	0.689	0.076	0.069	-1.604	0.714	0.029	0.032	-1.820	0.209
L2	4 46 11.1	-72 5 9.0	6.6	7.7	13	-2.163	-0.246	0.061	0.054	-2.051	-0.235	0.018	0.027	-1.910	0.181
L3	5 16 28.9	-68 37 1.8	6.6	7.1	45	-1.827	0.391	0.047	0.042	-1.798	0.320	0.014	0.016	-1.924	0.252
L4	5 16 36.8	-66 34 35.8	12.6	7.6	9	-1.781	0.196	0.083	0.093	-1.734	0.147	0.048	0.030	-1.974	0.100
L5	5 15 36.1	-70 54 0.8	-	1.9	41	-2.008	0.112	0.079	0.079	-	-	-	-	-1.767	0.143
L6	6 2 34.3	-68 30 41.1	13.3	7.2	8	-1.750	0.897	0.158	0.177	-1.664	1.058	0.045	0.055	-1.873	0.392
L7	5 16 26.3	-69 48 19.0	-	1.8	127	-1.942	0.226	0.053	0.053	-	-	-	-	-1.824	0.207
L8	5 0 54.0	-66 43 59.8	-	2.0	39	-1.883	-0.0232	0.062	0.062	-	-	-	-	-2.068	0.247
L9	4 53 56.5	-69 40 35.4	-	2.0	73	-1.985	-0.058	0.079	0.079	-	-	-	-	-1.892	0.394
L10	5 49 41.6	-69 44 15.1	-	1.9	65	-1.704	0.648	0.087	0.087	-	-	-	-	-1.802	0.062
L11	5 57 22.4	-67 13 21.5	2.9	6.6	8	-1.591	0.895	0.174	0.078	-1.664	0.814	0.041	0.031	-1.899	0.233
L12	5 1 46.7	-67 32 39.8	13.3	6.4	16	-1.903	-0.201	0.083	0.121	-1.817	-0.065	0.033	0.020	-1.980	0.231
L13	5 20 57.0	-70 24 52.6	-	1.5	85	-2.199	0.543	0.093	0.093	-	-	-	-	-1.980	0.409
L14	5 2 53.7	-67 25 45.0	13.3	7.1	18	-1.664	-0.091	0.108	0.140	-1.707	-0.054	0.034	0.031	-1.885	0.212
L15	5 14 12.1	-70 20 25.8	-	1.1	75	-2.512	0.553	0.127	0.127	-	-	-	-	-2.273	0.628
L16	5 4 36.0	-66 24 15.7	10.7	7.1	13	-1.561	0.166	0.063	0.077	-1.684	0.079	0.031	0.035	-1.890	0.270
L17	5 25 14.4	-65 54 45.7	-	1.2	17	-1.773	1.247	0.290	0.290	-	-	-	-	-2.009	1.081
L18	5 30 26.8	-66 48 52.9	-	1.6	22	-1.767	0.716	0.150	0.150	-	-	-	-	-2.001	0.434
L19	5 31 59.7	-69 19 51.5	-	1.1	114	-1.636	0.780	0.150	0.150	-	-	-	-	-1.706	0.340
L20	4 56 14.3	-67 39 9.0	-	2.5	48	-1.826	-0.139	0.057	0.057	-	-	-	-	-1.939	0.260
L21	5 10 32.5	-69 27 15.5	-	1.1	129	-2.042	-0.113	0.118	0.118	-	-	-	-	-1.964	0.043
L22	5 20 56.5	-65 39 4.8	17.7	6.9	23	-	-	-	-	-1.681	0.298	0.020	0.036	-1.914	0.206

**Note.** — The LMC field number, using the same notation as in K1, and RA/DEC for the QSOs (columns 1, 2 & 3). Column 4 lists the total exposure times in minutes for e3. Column 5 lists the time baseline, in years, between e1 and e3. Column 6 lists the number of stars used in the final transformations after all cuts and iterations have been applied. Columns 7–10 list the observed PMs and errors for the ACS reanalysis (see §2.3). Columns 11–14 list the corresponding observed PMs and errors obtained from the 3-epoch analysis (see §2.5). Columns 15 & 16 list the final COM PM estimates from each QSO field obtained from the procedure described in §3.2. Note that L22 is a new field, with only e1 and e3 data.

**Table 2**  
SMC Observations and PM Results

ID	RA	DEC	$T$	$\Delta time$	$N$	PM of FIELD AS OBSERVED								SMC PM(CM) estimate	
						$\mu_W$	$\mu_N$	$\delta\mu_W$	$\delta\mu_N$	$\mu_W$	$\mu_N$	$\delta\mu_W$	$\delta\mu_N$	$\mu_W$	$\mu_N$
	(H,M,S)	(deg, ', ")	(min)	(yr)		2-epoch PMs ( mas yr <sup>-1</sup> )				3-epoch PMs ( mas yr <sup>-1</sup> )				( mas yr <sup>-1</sup> )	
S1	00 51 17.0	-72 16 51.3	-	1.9	42	-0.682	-1.288	0.100	0.100	-	-	-	-	-0.738	-1.244
S2	00 55 34.7	-72 28 33.9	17.7	7.6	25	-0.748	-1.246	0.070	0.068	-0.722	-1.214	0.032	0.024	-0.760	-1.185
S3	01 02 14.5	-73 16 26.6	17.7	7.7	36	-0.893	-1.397	0.097	0.101	-0.679	-0.974	0.026	0.028	-0.691	-0.973
S4	00 36 39.7	-72 27 42.0	-	2.8	10	-0.460	-1.114	0.109	0.109	-	-	-	-	-0.579	-1.031
S5	01 02 34.7	-72 54 23.8	13.3	6.8	30	-1.046	-1.072	0.084	0.083	-0.806	-1.199	0.017	0.038	-0.815	-1.195

**Note.** — Same columns as in Table 1 but for the SMC.

**Table 3**  
Kinematical determinations of LMC geometry and rotation parameters

(1)	(2)	Paper II (3)	vdM02 (4)	Olsen11 (5)
inc	deg	$39.6 \pm 4.5$	$34.7 \pm 6.2^{[1]}$	$34.7 \pm 6.2^{[1]}$
theta	deg	$147.4 \pm 10.0$	$129.9 \pm 6.0$	$142 \pm 5$
RA	deg	$78.76 \pm 0.52$	$81.91 \pm 0.98$	$81.91 \pm 0.98^{[2]}$
DEC	deg	$-69.19 \pm 0.25$	$-69.87 \pm 0.41$	$-69.87 \pm 0.41^{[2]}$
$R_0^{[3]}$	kpc	$1.18 \pm 0.48$	$4.0 \pm 0.3^{[5]}$	$2.4 \pm 0.1$
$V_0^{[3]}$	km s <sup>-1</sup>	$76.1 \pm 7.6^{[4]}$	$49 \pm 2^{[5]}$	$87 \pm 5^{[6]}$
$v_{sys}$	km s <sup>-1</sup>	$262.2 \pm 3.4^{[7]}$	$262.2 \pm 3.4$	$263 \pm 2$
$m - M$	mag	$18.50 \pm 0.10^{[8]}$	$18.50 \pm 0.10^{[8]}$	$18.50 \pm 0.10^{[8]}$

**Note.** — Column (1) lists the following quantities: inclination of the LMC disk plane; position angle of the line of nodes; (RA,DEC) of the rotation center; turnover radius  $R_0$  and asymptotic velocity amplitude  $V_0$  of the rotation curve; systemic LOS velocity,  $v_{sys}$ ; and distance modulus,  $m - M$ . Column (2) lists the corresponding units. Column (3) lists the values inferred from the new PM data as described in Paper II. Columns (4) and (5) list the values inferred from the LOS velocity studies of vdM02 and Olsen et al. (2011).

<sup>[1]</sup> Value from van der Marel & Cioni (2001), used but not independently determined by vdM02 or Olsen et al. (2011).

<sup>[2]</sup> Value from vdM02, used but not independently determined by Olsen et al. (2011).

<sup>[3]</sup> The rotation curve is parameterized so that it rises linearly to velocity  $V_0$  at radius  $R_0$ , and then stays flat at larger radii.

<sup>[4]</sup> Applies to a mix of stellar populations (each with different asymmetric drift) as shown in Figure 6 of K1.

<sup>[5]</sup> Applies to (old) carbon stars (with large asymmetric drift). Determined from Table 2 of vdM02. Used an LMC COM PM value that pre-dates the now current HST values.

<sup>[6]</sup> Applies to (young) red supergiants (with little asymmetric drift). Used the LMC COM PM from P08.

<sup>[7]</sup> Value from vdM02, used but not independently determined in Paper II.

<sup>[8]</sup> Value from Freedman et al. (2001), used but not independently determined from kinematics.

**Table 4**  
Summary of Recent LMC and SMC PM Measurements

Work	LMC		SMC		Data
	$\mu_W$ (mas yr <sup>-1</sup> )	$\mu_N$ (mas yr <sup>-1</sup> )	$\mu_W$ (mas yr <sup>-1</sup> )	$\mu_N$ (mas yr <sup>-1</sup> )	
<b>This Paper</b>	<b>-1.910 ± 0.020</b>	<b>0.229 ± 0.047</b>	<b>-0.772 ± 0.063</b>	<b>-1.117 ± 0.061</b>	<b>HST 3-epoch</b>
( <i>vdM02 model</i> )	-1.899 ± 0.017	0.416 ± 0.017	...	...	HST 3-epoch
K1 & K2	-2.03 ± 0.08	0.44 ± 0.05	-1.16 ± 0.18	-1.17 ± 0.18	HST 2-epoch
P08	-1.956 ± 0.036	0.435 ± 0.036	-0.754 ± 0.061	-1.252 ± 0.058	HST 2-epoch
Costa et al.	-1.72 ± 0.13	0.50 ± 0.15	-0.93 ± 0.14	-1.25 ± 0.11	2.5m du Pont
Vieira et al. (2010)	-1.89 ± 0.27	0.39 ± 0.27	-0.98 ± 0.30	-1.10 ± 0.29	SPM

**Note.** — PMs of the LMC (columns 3 and 4) and SMC (columns 5 and 6) COM. Column (1) indicates the source of the result, and column (6) the type of data that was used. The first line (labeled “This Paper”) is the final result from the present paper, which uses the fit to the PM rotation field from Paper II. Ours is the first study that propagates the uncertainties in the geometry, center and rotation of each Cloud into the COM PM estimates. For this reason, other studies have generally underestimated their error bars. The second line shows the LMC COM PM estimate that is obtained when the LMC orientation and center are kept fixed to the same vdM02 values that were used by most other authors (see Section 4.1). For Costa et al. we list for the LMC the average of their 2009 results for  $V_{rot} = 50$  km/s and 120 km/s, respectively; for the SMC we list their 2011 result.

**Table 5**  
Galactocentric Velocities from *HST* measurements

Line	Galaxy	solar	PM	$v_X$ km/s	$v_Y$ km/s	$v_Z$ km/s	$v_{\text{tot}}$ km/s	$v_{\text{rad}}$ km/s	$v_{\text{tan}}$ km/s
(1)	<b>LMC</b>	<b>new</b>	<b>3-epoch</b>	<b>-57 ± 13</b>	<b>-226 ± 15</b>	<b>221 ± 19</b>	<b>321 ± 24</b>	<b>64 ± 7</b>	<b>314 ± 24</b>
(2)	LMC	IAU	3-epoch	-59 ± 12	-252 ± 15	221 ± 19	340 ± 23	86 ± 5	329 ± 24
(3)	LMC	new	3-epoch vdM02	-77 ± 8	-224 ± 14	227 ± 18	328 ± 23	65 ± 5	322 ± 24
(4)	LMC	IAU	3-epoch vdM02	-78 ± 8	-250 ± 14	227 ± 18	347 ± 23	87 ± 5	336 ± 24
(5)	LMC	IAU	P08	-83 ± 11	-258 ± 15	238 ± 20	361 ± 25	88 ± 5	350 ± 26
(6)	LMC	IAU	K1	-86 ± 14	-268 ± 18	252 ± 25	378 ± 31	89 ± 5	367 ± 31
(7)	<b>SMC</b>	<b>new</b>	<b>3-epoch</b>	<b>19 ± 18</b>	<b>-153 ± 21</b>	<b>153 ± 17</b>	<b>217 ± 26</b>	<b>-11 ± 5</b>	<b>217 ± 26</b>
(8)	SMC	IAU	3-epoch	18 ± 17	-179 ± 21	153 ± 17	236 ± 26	6 ± 4	236 ± 26
(9)	SMC	IAU	P08	23 ± 16	-197 ± 22	166 ± 17	259 ± 26	7 ± 4	259 ± 26
(10)	SMC	IAU	K2	-86 ± 49	-248 ± 46	150 ± 39	302 ± 57	23 ± 7	301 ± 57
(11)	<b>SMC-LMC</b>	<b>...</b>	<b>3-epoch</b>	<b>76 ± 22</b>	<b>73 ± 26</b>	<b>-68 ± 25</b>	<b>128 ± 32</b>	<b>112 ± 32</b>	<b>61 ± 16</b>
(12)	SMC-LMC	...	3-epoch vdM02	81 ± 19	73 ± 26	-89 ± 25	143 ± 31	134 ± 32	50 ± 15
(13)	SMC-LMC	...	P08	106 ± 20	61 ± 26	-72 ± 26	145 ± 30	136 ± 33	46 ± 18
(14)	SMC-LMC	...	K2	0 ± 51	20 ± 49	-103 ± 46	127 ± 46	77 ± 50	88 ± 45

**Note.** — The lines (1)–(6) list the LMC velocity, lines (7)–(10) the SMC velocity, and lines (11)–(14) the relative velocity of the SMC with respect to the LMC. Column (1) lists a line identifier. Column (2) lists the galaxy name. Column (3) lists the source of the velocities used to correct for solar reflex motion: “IAU” uses the IAU value of  $V_0 = 220 \text{ km s}^{-1}$  and the Dehnen & Binney (1998) solar peculiar velocity; “new” uses the improved McMillan (2011) value of  $V_0 = 239 \pm 5 \text{ km s}^{-1}$  and the improved Schönrich et al. (2010) solar peculiar velocity. Column (4) lists the assumed PM value, taken from the list of observations in Table 4: “3-epoch” corresponds to the line labeled “This Paper” (which uses the new data with the LMC geometry fit from Paper II, with uncertainties included); “3-epoch vdM02” corresponds to the line labeled “(vdM02 model)” (which uses the new data with the fixed geometry parameters from vdM02). Columns (5)–(7) list the Galactocentric velocity coordinates ( $v_X, v_Y, v_Z$ ). Columns (8)–(10) lists the total length of the velocity vector, the radial component, and the transverse component, respectively. Uncertainties were calculated using a Monte-Carlo scheme that propagates all relevant uncertainties in the position and velocity of both the Clouds and the Sun. Distance uncertainties are based on  $\Delta m - M = 0.1$ . Velocity uncertainties in the Galactocentric frame are highly correlated, because uncertainties in the LOS direction are much smaller than in the transverse direction.

**Table 6**  
MW and LMC Properties

Galaxy	Total Mass [ $M_\odot$ ]	$c_{\text{vir}}$	$R_{\text{vir}}$ [kpc]	$M_{\text{disk}}$ [ $M_\odot$ ]	Plummer Softening [kpc]
MW	$1 \times 10^{12}$	9.86	261	$6.5 \times 10^{10}$	-
MW	$1.5 \times 10^{12}$	9.56	299	$5.5 \times 10^{10}$	-
MW	$2 \times 10^{12}$	9.36	329	$5.0 \times 10^{10}$	-
LMC	$3 \times 10^{10}$	-	-	-	8
LMC	$5 \times 10^{10}$	-	-	-	11
LMC	$8 \times 10^{10}$	-	-	-	14
LMC	$1 \times 10^{11}$	-	-	-	15
LMC	$1.8 \times 10^{11}$	-	-	-	20
LMC	$2.5 \times 10^{11}$	-	-	-	22.5

**Note.** — Different MW and LMC mass models used in the orbital calculations.  $c_{\text{vir}}$  is the halo concentration, and  $R_{\text{vir}}$  is the virial radius of the MW in each case. The mass of the MW bulge is kept fixed at  $1 \times 10^{10} M_\odot$  and the Hernquist scale radius for the MW bulge is kept fixed at 0.7 kpc. The MW’s exponential disk scale radius is kept fixed at 3.5 kpc. The mass of the MW disk is varied to get the observed circular velocity at the solar circle as discussed in the text.